Geophysical Journal International

Geophys. J. Int. (2023) **232,** 1236–1258
Advance Access publication 2022 October 07
GJI Seismology

https://doi.org/10.1093/gji/ggac387

Calibration of a Bayesian spatio-temporal ETAS model to the June 2000 South Iceland seismic sequence

Atefe Darzi [1], Benedikt Halldorsson,[1,2] Birgir Hrafnkelsson,[3] Hossein Ebrahimian,[4] Fatemeh Jalayer[4,5] and Kristín S. Vogfjörð[2]

[1] *Faculty of Civil and Environmental Engineering, School of Engineering and Natural Sciences, University of Iceland,* 107 *Reykjavík, Iceland.*
E-mail: atefe@hi.is
[2] *Division of Processing and Research, Icelandic Meteorological Office,* 150 *Reykjavík, Iceland*
[3] *Faculty of Physical Sciences, University of Iceland,* 102 *Reykjavik, Iceland*
[4] *Department of Structures for Engineering and Architecture, University of Naples Federico II,* 80138 *Napoli NA, Italy*
[5] *Institute for Risk and Disaster Reduction (IRDR), Faculty of Maths and Physical Sciences, University College London (UCL)*

Accepted 2022 October 3. Received 2022 September 29; in original form 2021 August 4

SUMMARY

The reliable forecasting of seismic sequences following a main shock has practical implications because effective post-event response is crucial in earthquake-stricken regions, aftershocks can progressively cause increased damage and compound economic losses. In the South Iceland Seismic Zone (SISZ), one of two large transform zones in Iceland where earthquake hazard is the highest, an intense seismic sequence took place during 17–24 June 2000, starting with a M_w 6.4 main shock on 17 June 2000, followed by another M_w 6.5 main shock four days later and on a different fault. Both earthquakes caused considerable damage and incurred heavy economic losses. They were immediately followed by intense aftershock activity on the causative faults and triggered earthquakes as far as 80 km away along the transform zone. To investigate the feasibility of forecasting the progression of such complex sequences, we calibrated a spatio-temporal epidemic-type aftershock sequence (ETAS) clustering model to the June 2000 seismic sequence in the framework of Bayesian statistics. Short-term seismicity forecasts were carried out for various forecasting intervals and compared with the observations, the first generated a few hours after the first main shock and followed by daily forecasts. The reliability of the early forecasts was seen to depend on the initial model parameters. By using an adaptive parameter inference approach where the posteriors from each preceding forecasting interval served as informative priors for the next, the fast convergence of the parametric values was ensured. As a result, the 16–84 percentile range of the forecasted number of events captured the actual number of observed events in all daily forecasts, and the model exhibited a strong spatial forecasting ability, even only a few hours after the main shock, and over all subsequent daily forecasts. We present the spatio-temporal ETAS parameters for the June 2000 sequence as ideal candidates of prior estimates for future operational earthquake forecasting of other Icelandic aftershock sequences. Past seismic sequences need to be analysed retrospectively to confirm the stability of the parameters of this study, effectively enable the application of the Bayesian ETAS model as an operational earthquake forecasting system for aftershocks in Iceland.

Key words: Probabilistic forecasting; Statistical methods; Earthquake interaction, forecasting, and prediction; Bayesian inference; Operational earthquake forecasting.

1 INTRODUCTION

Iceland is the most seismically active region in northern Europe. The interplay of the mid-Atlantic ridge, an extensional boundary between the Eurasian and North American tectonic plates, and the Icelandic hot spot, a localized upwelling of mantle material, is responsible for the intense seismic and volcanic activity in Iceland. An eastward ridge-jump on land has formed two major transform zones, the South Iceland Seismic Zone (SISZ) in the south and the Tjörnes Fracture Zone (TFZ) in the north which also extends offshore (Fig. 1; Einarsson 1991, 2014; Rögnvaldsson *et al.* 1998; Stefánsson *et al.* 2008). Historically, the most destructive earthquakes and intense seismic sequences in Iceland

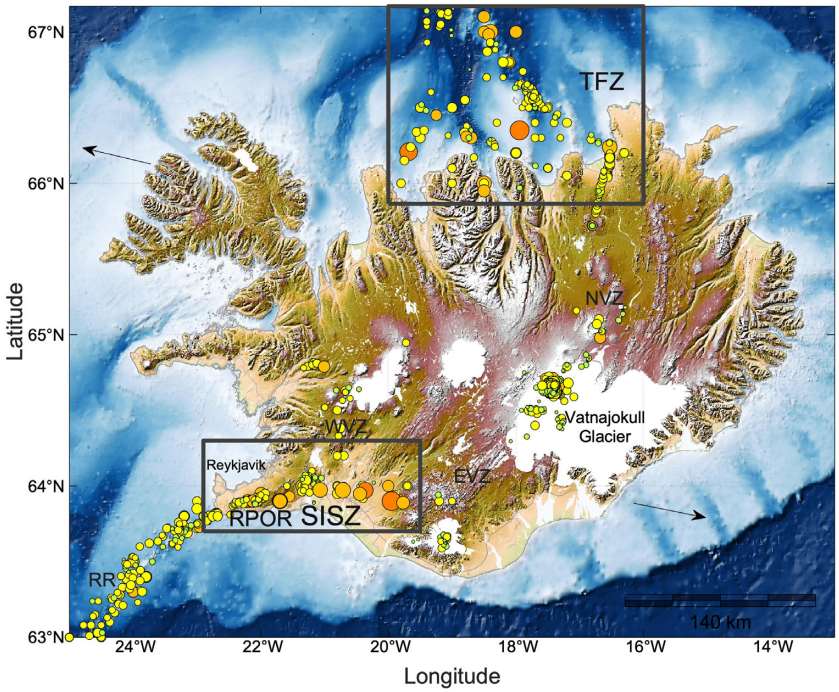

Figure 1. A map of Iceland's topography and bathymetry, showing the spatial distribution of significant earthquakes ($\boldsymbol{M} \geq 3.3$) in Iceland from 1904 to 2019 (coloured circles, with darker colours and larger symbols denoting relatively larger earthquakes; Jónasson *et al.* 2021) with emphasis on the two transform zones of the country, the SISZ-RPOR and TFZ where strike-slip earthquakes dominate (see text). The location of the capital region of Reykjavik is also indicated, along with the key southwest–northeast aligning volcanic zones where active tectonic extension dominates: the offshore Reykjanes Ridge (RR), the Western Volcanic Zone (WVZ) and the Eastern Volcanic Zone (EVZ). The Northern Volcanic Zone (NVZ) is aligned from north to south primarily. The arrows indicate the approximate direction of plate motions of the North American and (left-hand side) and Eurasian (right-hand side) tectonic plates, respectively.

have occurred in these transform zones, in particular the SISZ and TFZ (Einarsson 1991, 2010, 2014; Stefánsson *et al.* 1993, 2008; Metzger & Jónsson 2014; Einarsson *et al.* 2020; Steigerwald *et al.* 2020). Thus, the seismic hazard in Iceland is highest in these zones with design peak ground accelerations of 0.50 g associated with 10 per cent probability of exceedance in 50 years (Standards Council of Iceland 2010). The SISZ coincides with a relatively densely populated agricultural region that contains all critical infrastructure of a modern-day society such as towns, roads, bridges, industrial companies, power plants (geothermal and hydropower) and lifeline networks. Notably, towards the west the transform fault system of the SISZ extends all along the Reykjanes Peninsula Oblique Rift (RPOR, see Fig. 1; Steigerwald *et al.* 2020). The dense concentration of ∼2/3 of the country's population in the nearby capital region of Reykjavik exposes it to the hazard of the seismogenic faults of the SISZ and RPOR, making this part of the country the region of highest seismic risk in Iceland [see Darzi *et al.* (2022a) for detail seismic risk assessment for an earthquake scenario of M_w 6.3 May 2008 in SISZ].

While historical earthquake catalogues for the entire Iceland indicate that the average annual frequency of occurrence of M_w 6 or larger is ∼0.06–0.07 (i.e. every ∼15 yr), the fact is that the occurrence of strong earthquakes in Iceland is highly episodic and reveals significant clustering in time (and space). For example, intense sequences of moderate-to-strong earthquakes repeatedly take place in the SISZ, with multiple main shocks over a period lasting from a few weeks to a few years or a couple of decades (Einarsson 2014). One of the most recent intense seismic sequences was the June 2000 sequence during which the two largest Icelandic earthquakes took place in SISZ with less than 4-d time interval. The June 2000 sequence started abruptly by the first main shock occurred on 17 June 2000 with M_w 6.4 and the second one happened on 21 June 2000 with M_w 6.5. Both main shocks were followed by a period of intense aftershock activity on the causative faults in addition to multiple dynamically triggered events larger than M_w 5 that occurred immediately after the first main shock on 17 June (Árnadóttir *et al.* 2001, 2006; Pagli *et al.* 2003; Pedersen *et al.* 2003; Sigbjörnsson & Ólafsson 2004).

Over the last decade, the earthquake forecasting research has shown that it is becoming increasingly more feasible to forecast the spatio-temporal evolution of seismic sequences, that is aftershocks triggered after a strong earthquake main shock (Zhuang *et al.* 2002; Ogata & Katsura 2006; Console *et al.* 2010; Llenos & Michael 2017; Marzocchi *et al.* 2017; Schorlemmer *et al.* 2018; Taroni *et al.* 2018). This has practical importance because the aftershocks can progressively cause increased damages and economic losses, and effective post-event response is crucial to reduce such losses in the earthquake-stricken regions. For example, the 2011 M_w 9.0 Japan earthquake and tsunami was preceded by a M_w 7.3 earthquake 2 d earlier (Nanjo *et al.* 2013; Ogata *et al.* 2013). On a short timescale, earthquake sequences show a high degree of clustering in space and time, meaning that the probability of triggering increases with initial shock's magnitude and decays with elapsed time. Understanding the clustering pattern and the statistical features observed in earthquake catalogues is expected to improve forecasts indicating changes in the short-term earthquake probability (Jordan *et al.* 2011).

Earthquake clustering and triggering models used in aftershock forecasting can be applied to short-term earthquake forecasting. The first generation of operational earthquake forecasting (OEF) models used for short-term clustering of earthquakes was mostly based on statistical evaluation of seismicity. For instance, Reasenberg & Jones (1989) introduced a seismicity model to forecast aftershock decay rate after a large main shock based on a combination of two universal empirical laws, the Omori-Utsu (Omori 1894; Utsu 1961; Utsu & Ogata 1995) and the Gutenberg–Richter (Gutenberg & Richter 1944) which are the strongest relations in statistical seismology. The so-called Modified Omori (MO, Utsu 1961) model has been used widely to generate automated alerts following moderate earthquakes in California (Field *et al.* 2016). Recently, Jalayer *et al.* (2011), Ebrahimian *et al.* (2014), Page *et al.* (2016) and Hardebeck *et al.* (2019) improved the performance of MO seismicity model using the Bayesian updating of the model parameters. However, the MO model suffers from several deficiencies. For example, the model assumes all aftershocks are triggered by the main shock which is not an accurate assumption (e.g. second-order triggering), the model does not include spatial information (see Ebrahimian *et al.* 2014 for including a spatial term to MO model) and performs poorly for complex seismic sequences and swarms of multiple similar-sized events (Marzocchi *et al.* 2017).

Most OEF systems appear in recent years to be converging towards an Epidemic-Type Aftershock Sequence (ETAS) model (Harte 2014, 2017, 2019; Marzocchi *et al.* 2014; Omi *et al.* 2014; Field *et al.* 2017) which is a space–time–magnitude clustering model, initially introduced by Ogata (1998). According to several studies (Marzocchi & Lombardi 2009; Schorlemmer *et al.* 2018; Taroni *et al.* 2018; Nandan *et al.* 2019), the ETAS model ranks top amongst the best models of earthquake forecasting developed to date and particularly outperforms other statistical and physics-based models of seismicity (Console *et al.* 2007; Taroni *et al.* 2018). Contrary to MO model, the ETAS model is capable of forecasting the evolution of complex seismic sequences (e.g. 2016–2017 Amatrice-Norcia) and accounts for secondary aftershock sequences, that is for sequences with large enough aftershocks that can trigger many of their own aftershocks (Ebrahimian & Jalayer 2017; Llenos & Michael 2017; Marzocchi *et al.* 2017; Nandan *et al.* 2019).

Recently, Douglas & Azarbakht (2020) indicated that an OEF system could be cost-beneficial for high seismic hazard regions such as Iceland through low-cost, short-term mitigation actions (i.e. costing less than 0.1 per cent of the mitigated losses) that can be performed before a large impending earthquake (if the increase in the weekly forecasted seismicity is moderate). In general, OEF systems mainly find application in seismic regions where dense regional earthquake monitoring network are in place and capable of real-time earthquake detection, even during intense earthquake sequences, for example aftershocks after a strong main shock or triggered earthquakes in the region. The national seismic network started in 1991 in the South Iceland Lowland (SIL) by the Icelandic Meteorological Office (IMO) and detects and records earthquakes with a very low earthquake magnitude of completeness in the SISZ due to both its dense distribution of stations and its effective phase correlation algorithm (Stefánsson 2020). As a result, a complete high-quality SIL data set of seismic data for SW-Iceland exists and thus provides a unique opportunity to explore the feasibility, limits and benefits of an OEF system for southwest Iceland by retrospectively analysing its sequences in a systematic way.

While a prototype OEF system based on an ETAS model proposed by Eberhard (2014) has been run internally at the IMO since December 2014 for the SISZ and RPOR, it has not found practical use. Moreover, it suffers from several shortcomings such as (i) covering only southwest Iceland with a relatively large spatial grid size of 0.025°, (ii) use of earthquake catalogue from the broad range of 1991–2006 from the whole Iceland to determine the ETAS model parameters, thus ignoring the potential effects of different learning time intervals, (iii) using constant model parameters and (iv) ignoring model parametric uncertainty (Eberhard 2014).

These are significant shortcomings as several studies have shown that the estimation of ETAS model parameters is both challenging and is subjected to a large amount of uncertainty (Lombardi 2017; Shcherbakov *et al.* 2018). Nevertheless, majority of ETAS applications run based on the plug-in estimates (i.e. using maximum likelihood point estimates for model parameters) and thus, provide the probability of an upcoming large aftershock without considering the uncertainties in the estimation of the model parameters. Particularly, the large model parameter uncertainty applies in the early aftershock period can be primarily caused by detection and recording problems and thereby substantial deficiency of data (Omi *et al.* 2013; Seif *et al.* 2017). Therefore, it is critical to take heed of the uncertainty of the ETAS parameter estimation and in that respect, the Bayesian statistical framework appears to be ideal as it allows the use of prior distributions of model parameters to explicitly evaluate their posterior distributions and their uncertainty therefore to be explicitly quantified. There have been only a few studies on the Bayesian-based ETAS model parameter updating (Jalayer & Ebrahimian 2014; Ebrahimian & Jalayer 2017; Kolev & Ross 2019; Shcherbakov *et al.* 2019; Convertito *et al.* 2021; Ross 2021). Then, Ebrahimian & Jalayer (2017) proposed a fully simulation-based and robust framework for providing the spatio-temporal distribution of the events that are going to happen in a prescribed forecasting time interval after the main shock. This method captures the uncertainties in the ETAS model parameters and simulates the seismic events that can occur during the forecasting time interval of interest. They provided retrospective forecasting for 2016 Amatrice seismic sequence in central Italy and illustrated promising results. This workflow was successfully applied to the earthquake sequences between 1995 and 2018 in Greece (Azarbakht *et al.* 2022) as well as induced seismicity of St Gallen deep geothermal field in Switzerland (Convertito *et al.* 2021). Most recently, in Iceland, Darzi *et al.* (2022b) assessed the forecasting capability of the method to predict the upcoming earthquakes in space and different short time intervals during several stages that commenced with the damaging 29 May 2008 Ölfus earthquake (M_w 6.3) in SISZ.

In this study, we calibrate a Bayesian spatio-temporal ETAS model to the June 2000 seismic sequence in the SISZ and RPOR in SW-Iceland and present the model parameters along with their corresponding uncertainties. On that basis we explore the forecasting capabilities of the model both for providing the spatial distribution forecasts as well as the total number of forecasted events larger than a specific cut-off magnitude, for a range of short-term forecasting time intervals of various start times and durations. We present the corresponding distributions of forecasted number of aftershocks and compare with the actual observations. We then assess the sensitivity of the posterior distributions

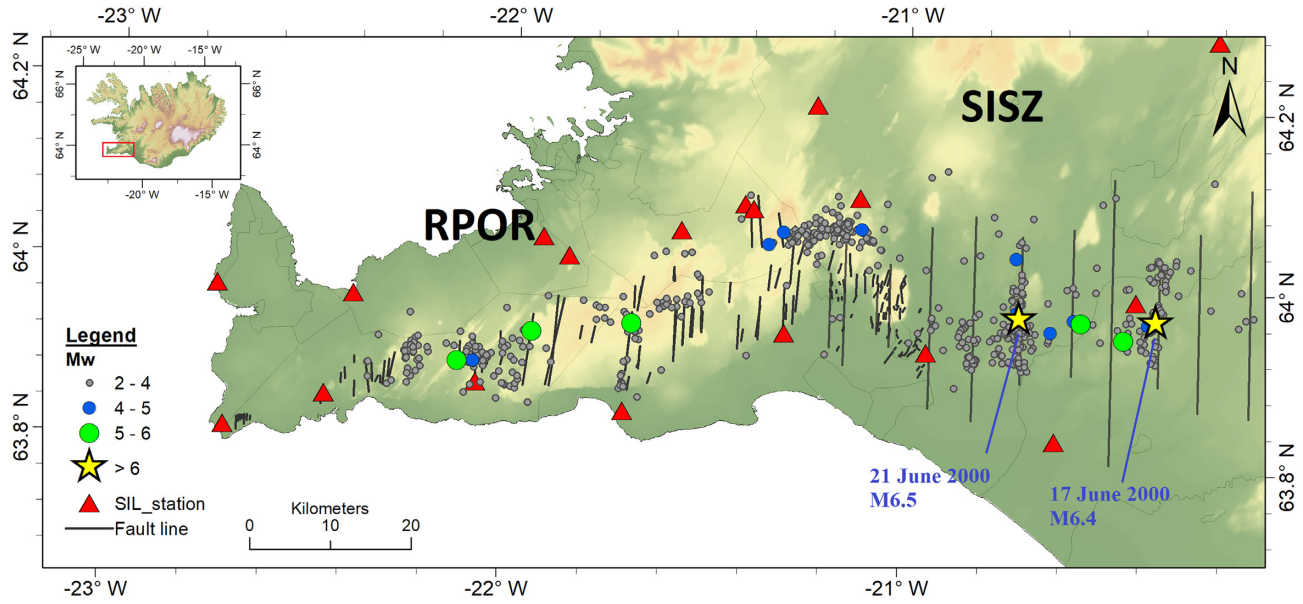

Figure 2. Geographical distribution of the June 2000 earthquake sequence in the SISZ and RPOR. Earthquakes with $M \geq 2.0$ occurred from 17 June up to 25 June 2000 are plotted. Note that data are from the earthquake catalogue provided by Panzera *et al.* (2016). Red triangles depict Icelandic Seismic Network (SIL) stations. The surface expressions of past transform faulting lines are reproduced, from Einarsson (2014), Einarsson *et al.* (2020) and Steigerwald *et al.* (2020), in the RPOR and western SISZ. The straight north–south lines in the central and eastern SISZ schematically indicate the extents of large earthquakes, inferred by Roth (2004).

of the spatio-temporal ETAS model to various initial prior values to scrutinize the reliability of the forecasts. We present the optimal set of parameters that are recommended as informative priors for any spatio-temporal Bayesian seismicity forecasts of future seismic sequences.

2 THE JUNE 2000 EARTHQUAKE SEQUENCE IN THE SISZ

Instead of a long and narrow sinistral transform zone along the East to West axis of the SISZ and RPOR transform zones, the causative faults of strong earthquakes in the zones are dextral, striking north to south. The faults form an array of densely spaced, short parallel and near-vertical strike-slip faults (see Fig. 2). In addition, the strike-slip faults of the RPOR intersect several SW–NE striking volcanic fissure swarms. The faults indicated in Fig. 2 by straight and long N–S black lines are the estimated surface fault projections of large historical earthquakes in the SISZ (Roth 2004), while shorter lines indicate mapped surface fractures associated with transform faults in the SISZ and RPOR (Einarsson 2014; Einarsson *et al.* 2020; Steigerwald *et al.* 2020).

The seismogenic potential of the SISZ and RPOR varies systematically, with the largest historical earthquake of $M_w \sim 7.0$ having occurred in the easternmost part of the SISZ in 6 May 1912 (Bjarnason *et al.* 1993; Bellou *et al.* 2005; Jónasson *et al.* 2021). The plate movement in SW-Iceland is thus considered capable of producing earthquakes in the magnitude range 6–6.5 with return periods of a few decades (Einarsson 1991, 2010, 2014; Sigmundsson *et al.* 1995; Sigmundsson 2006; Einarsson *et al.* 2020; Steigerwald *et al.* 2020). However, the occurrence of strong earthquakes in Iceland is highly episodic as they are usually followed by a period of intense aftershock activity and moderate-to-strong triggered earthquakes over the transform zones. An example is the major sequence that occurred during 1896–1912 resulting in six earthquakes that were distributed along the entire length of the SISZ. Then, over the last few decades, moderate-to-strong tectonic earthquakes have taken place in the SISZ including the 25 May 1987 Vatnafjöll (M_w 6.0), 4 June 1998 (M_w 5.5), 17 June 2000 (M_w 6.4, M_w 5.7), 21 June 2000 (M_w 6.5) and 29 May 2008 (M_w 6.3) earthquakes.

Fig. 2 shows the June 2000 seismic sequence from 17 June 2000 to 25 June 2000 with $M > 2.0$ that occurred in the SISZ and RPOR. At 15:40 UTC on 17 June 2000, a M_w 6.4 earthquake occurred in the eastern part of the SISZ (shown with a yellow star in Fig. 2), immediately followed by an intense aftershock sequence on and around the causative fault. Two M_w 5.7 earthquakes in the SISZ (shown with green circles in SISZ in Fig. 2) and one M_w 5.7 earthquake in eastern SISZ (the rightmost green circle in RPOR in Fig. 2 happened less than 2 min since the 17 June main shock. The aftershocks extended 80 km to the west in central RPOR (see Fig. 2). Three and a half days after the first main shock, at 00:51 UTC on 21 June 2000, a M_w 6.5 earthquake occurred on a neighbouring fault (see the yellow star in Fig. 2) in central SISZ. These two strong events took place on two separate but parallel near-vertical north-striking transform faults located approximately 18 km apart and caused damage in the nearby towns and rural farmhouses (Sigbjörnsson & Ólafsson 2004). The seismicity increased significantly in the whole of southwestern Iceland, with thousands of microearthquakes (i.e. having moment magnitude smaller than around 2) recorded by the SIL network associated with the activation of ∼90 km of the plate boundary (Hjaltadóttir 2009), while the seismic triggering was attributed to dynamic processes (i.e. wave propagation) (Antonioli *et al.* 2006). Although both main shocks were followed by intense aftershock sequences, the seismicity rate decayed considerably fast. It has been noted that the June 2000 earthquakes occurred after almost nine decades of relative

quiescence since the major sequence of 1896–1912, but are estimated to only having released one-fourth of the strain accumulated across the SISZ since then (Árnadóttir 2004; Einarsson 2014).

A complete parametric catalogue for southwest Iceland of earthquakes recorded by the SIL network from 1991 to 2013 has been assembled and revised by Panzera *et al.* (2016). This catalogue forms the basis of the analysis carried out in this study. The recording sites of the SIL network are shown as red triangles in Fig. 2.

Fig. 3(a) shows the magnitude-time progression for $M \geq 1.0$ of the entire catalogue starting from 10 June until 25 June 2000. Note that no notable events preceded the M_w 6.4 earthquake at 15:40:41 UTC on 17 June 2000. Fig. 3(b) then shows the temporal evolution of the daily number of earthquakes with $M \geq 2.0$ (left-hand axis) from 17 to 25 June (shown with blue circles) illustrating also the distribution of their magnitudes lumped per day (right axis) which are depicted by red circles proportional in size to their corresponding moment magnitude. A total of 280 earthquakes with $M \geq 2.0$ occurred on 17 June and more than 100 events occurred on 18 and 21 June 2000. The seismicity decays rather fast as the sequence of significant aftershocks appears to last only a few days.

3 THE SPATIO-TEMPORAL SEISMICITY FORECASTING FRAMEWORK

3.1 Theoretical concept

The spatio-temporal ETAS model describes the earthquake occurrence rate by a non-homogenous Poisson point process as a function of magnitude, space and time. This seismicity occurrence model is used herein to perform robust seismicity forecasting by using the Bayesian parameter estimation technique (Ebrahimian & Jalayer 2017).

$$N\ (x, y, m|\mathbf{seq},\ M_{\text{cut}}) = N_{\text{b}}\ (x, y, m|\ M_{\text{cut}}) \quad + \int_{T_{\text{start}}}^{T_{\text{end}}} \lambda_{\text{ETAS}}(t, x, y, m|\mathbf{seq},\ M_{\text{cut}})\text{d}t. \tag{1}$$

The conditional number of earthquakes (denoted as N) is calculated based on two terms shown on the right-hand side of eq. (1). The first term is the background seismicity (N_{b}) which is often considered to be time-independent indicating the long-term seismicity; it is assumed to be caused by the similar underlying process such as seismotectonic movement. The second term quantifies the number of events with potential of triggering offspring of its own during a specific forecasting time interval, denoted as $[T_{\text{start}}, T_{\text{end}}]$, based on the aftershock triggering function. T_{start} and T_{end} are the starting and ending times of issuing forecast. $\lambda_{\text{ETAS}}(t, x, y, m|\mathbf{seq},\ M_{\text{cut}})$ expresses the conditional rate of occurrence of earthquakes with magnitude equal to or above m at time t elapsed after T_0 (where T_0 is the origin time of the seismic sequence of interest) within a spatial cell with the central location of (x, y) located within the aftershock zone using ETAS model. This rate is conditioned on the lower cut-off magnitude, denoted as M_{cut}, as well as the observation history, denoted as **seq** hereafter, which indicates the sequence of events available at the time of forecast. Note that **seq** is comprised of N_0 number of events including the main shock and series of aftershocks (or foreshocks) that took place in the time interval $[T_0, T_{\text{start}})$. The mathematical expression can be $\mathbf{seq} = \{(t_i, x_i, y_i, M_i), T_0 < t_i < T_{\text{start}},\ M_i \geq M_{\text{cut}},\ i = 1 : N_0\}$, where t_i is the arrival time for the ith event with magnitude M_i and location (x_i, y_i). M_{cut} is the magnitude equal to or greater than the completeness magnitude of the **seq**. The calculation of the number of events in eq. (1) will be further expanded and explained in Section 3.2 (see eq. 3). Thus, we have:

$$\lambda_{\text{ETAS}}\ (t, x, y, m|\boldsymbol{\theta}, \mathbf{seq}_t,\ M_{\text{cut}}) = \text{e}^{-\beta(m-M_{\text{cut}})} \sum_{t_j<t} \left[K\text{e}^{\beta\left(M_j-M_{\text{cut}}\right)} \frac{K_{\text{t}}}{\left(t-t_j+c\right)^p} \frac{K_{\text{R}}}{\left(r_j^2+d^2\right)^q} \right]. \tag{2}$$

As can be seen in eq. (2), λ_{ETAS} represents the spatio-temporal ETAS triggering function which presents the influence of registered seismicity with $t_j < t$. It consists of three main empirical functions as follows: (1) the magnitude-dependent aftershock productivity by a parent earthquake associated with the Gutenberg–Richter relationship, characterized by parameter β. It is noteworthy that in the ETAS model used herein, the triggering ability coefficient, α, with the dimension magnitude^{-1} is assumed to be equal to the parameter β. This assumption is discussed in detail in Papadopoulos *et al.* (2021). In summary, in case of spatio-temporal ETAS models (such as the present study), the value of α can be significantly underestimated because of four possible reasons: (i) aftershock incompleteness (Hainzl *et al.* 2013), (ii) excessive smoothing of the background distribution (Harte 2013), (iii) potential time-dependence of the background rate (Hainzl *et al.* 2013) and (iv) the adoption of an isotropic kernel for the aftershock distribution (Hainzl *et al.* 2008). As a result, a common practice to avoid any of the above potential bias is to impose $\alpha = \beta$ which is the assumption taken in the current study that can also reduce the number of ETAS parameters that are going to be updated through the Bayesian method. See Convertito *et al.* (2021) for an updated version of the same ETAS model where the conditional aftershock triggering rate α is distinguished from Gutenberg–Richter seismicity parameter β; (2) the temporal decay of aftershocks defined by the Omori–Utsu law, characterized by parameters c and p and (3) the spatial decay of aftershocks relative to the epicentre of the parent event, characterized by parameters d and q. Parameters K, K_{R} and K_{t} satisfy the achievement of asymptotic compatibility between ETAS predictions and the long-term seismicity. In total, the spatio-temporal ETAS model parameters, denoted as $\boldsymbol{\theta}$, includes a vector of $[\beta,\ c,\ p,\ d,\ q,\ K,\ K_{\text{R}},\ K_{\text{t}}]$.

As mentioned above, $\mathbf{seq}_t$ corresponds to the observed events in the catalogue with magnitude equal to or greater than M_{cut} that happened up to the time t. In other words, $\mathbf{seq}_t = \{(t_j, x_j, y_j, M_j), t_j < t,\ M_j \geq M_{\text{cut}}\}$, where j is the index for events in $\mathbf{seq}_t$ with the arrival time t_j, the epicentre coordinates (x_j, y_j) and magnitude M_j. The r_j is the distance between each event j and the point (x, y). Note that events with $M_j \geq M_{\text{cut}}$ are assumed to have the potential of triggering aftershocks of their own.

3.2 Seismicity forecasting framework

The robust earthquake forecasting framework used herein is based on the ETAS model, and results in spatial distribution of seismicity as well as the number of events with magnitudes larger than a desired threshold for a target forecasting time interval. It is used for a range of short-term forecasting time interval (in order of hours to days) during the June 2000 seismic sequence.

To this end, the aftershock zone (the region affected by the main shock as well as its subsequent aftershocks) should be divided into smaller cell units creating a mutually exclusive and collectively exhaustive subset of grid cells. Considering a specific short-term forecasting time interval presented by $[T_{\text{start}}, T_{\text{end}}]$ in eq. (2), the lower cut-off magnitude, M_{cut}, is determined based on the completeness magnitude of the subcatalogue of all events registered in the time window $[T_0, T_{\text{start}})$. Then, **seq** can be selected from this subcatalogue by segregating events with $M_j \geq M_{\text{cut}}$. Afterwards, given known **seq** and M_{cut}, a robust estimate of the average number of events (E[N]) in the spatial cell unit centred at (x, y) with magnitude $m \geq M_{\text{cut}}$ in the forecasting interval $[T_{\text{start}}, T_{\text{end}}]$ is calculated over the domain of the model parameters $\Omega_{\boldsymbol{\theta}}$ as follows (eq. 2) is altered to eq. (3):

$$\mathrm{E}\left[N\left(x, y, m|\ \mathbf{seq},\ M_{\text{cut}}\right)\right] = N_{\text{b}}\left(x, y, m|M_{\text{cut}}\right) + \int_{\Omega_{\boldsymbol{\theta}}}\left[\int_{\Omega_{\mathbf{seq_g}}}\int_{T_{\text{start}}}^{T_{\text{end}}}\left(\lambda_{\text{ETAS}}(t, x, y, m|\mathbf{seq_g}, \boldsymbol{\theta}, \mathbf{seq},\ M_{\text{cut}})\mathrm{d}t\right).p(\mathbf{seq_g}|\boldsymbol{\theta}, \mathbf{seq},\ M_{\text{cut}})\mathrm{d}\mathbf{seq_g}\right] .p(\boldsymbol{\theta}|\mathbf{seq},\ M_{\text{cut}})\mathrm{d}\boldsymbol{\theta}, \tag{3}$$

where $p(\boldsymbol{\theta}|\mathbf{seq},\ M_{\text{cut}})$ is the conditional (posterior) probability distribution function (PDF) for $\boldsymbol{\theta}$ given the **seq** and M_{cut}. The robust estimate for the average number of aftershock events also considers all the plausible sequences of events $\mathbf{seq_g}$ (with the domain $\Omega_{\mathbf{seq_g}}$) that can happen during the forecasting time interval. Thus, $p(\mathbf{seq_g}|\boldsymbol{\theta}, \mathbf{seq},\ M_{\text{cut}})$ is the PDF for $\mathbf{seq_g}$ given $\boldsymbol{\theta}$, **seq** and M_{cut} are known. We note that the integral with respect to time in eq. (3) cannot be calculated analytically over the entire $[T_{\text{start}}, T_{\text{end}}]$, thus approximated by summing over the subintervals of $[t_{i-1}, t_i]$ within the generated sequence $\mathbf{seq_g}$ (see eq. 10 in Ebrahimian & Jalayer 2017). The rate λ_{ETAS} is estimated over the sequence of events that precede T_{end}, that is $\{\ \mathbf{seq}, \mathbf{seq_g}\}$, knowing that **seq** remains unchanged (observed data) among plausible samples. Hence, a robust estimate for the average number of events can be obtained based on plausible model parameters $\boldsymbol{\theta}$ as per eq. (3) according to the following steps:

Step 1: First and foremost, we define a prior distribution for the ETAS model parameters. There are two options for choosing the initial estimates of the ETAS parameters: we can either use the ETAS parameters proposed by previous studies for the region under investigation if available or use non-informative prior information.

It should be highlighted that although, the vector of ETAS model parameters $\boldsymbol{\theta}$ includes eight parameters, namely $[\beta,\ c,\ p,\ d,\ q,\ K,\ K_{\text{R}},\ K_{\text{t}}]$, the first five parameters are 'learned' through Bayesian inference. In fact, parameters K, K_{R} and K_{t} are calculated directly as a function of the rest of the parameters (see eqs 4–6) satisfying three conditions to reach the compatibility that the integral of λ_{ETAS} over infinite space and time needs to converge in limit to the number of earthquakes estimated by the Gutenberg–Richter model with $M > m$ (for detail information see Ebrahimian & Jalayer 2017). The K_{t} and K_{R} are determined such that the integrating the temporal decay term and spatial term of the ETAS, respectively, over infinite time and space, will in limit be equal to unity. Moreover, K is calibrated such that the number of events with $M \geq M_{\text{cut}}$ happened in $[T_0, T_{\text{start}}]$ across the entire aftershock zone is equal to the total number of events included in **seq**. Thus, five model parameters $[\beta,\ c,\ p,\ d,\ q]$ are used in the updating framework herein.

$$K_{\text{t}} = (p-1)\ c^{p-1},\quad p > 1 \tag{4}$$

$$K_{\text{R}} = \frac{(q-1)}{\pi}\, d^{2(q-1)},\quad q > 1 \tag{5}$$

$$K\ = \frac{N_0}{\int_{T_0}^{T_{\text{start}}}\left[\sum_{t_j<t}\frac{K_{\text{t}}.e^{\beta\left(M_j - M_{\text{cut}}\right)}}{\left(t-t_j+c\right)^p}\right]\mathrm{d}t}\ . \tag{6}$$

Step 2: In this step, having **seq** and M_{cut}, samples of $\boldsymbol{\theta}$ are generated from the posterior PDF $p(\boldsymbol{\theta}|\mathbf{seq},\ M_{\text{cut}})$ using an advanced simulation technique. To this end, we use the Markov Chain Monte Carlo (MCMC) simulation routine (Beck & Au 2002) based on a Metropolis–Hastings algorithm (Metropolis *et al.* 1953; Hastings 1970). It should be emphasized that the first 10 per cent of the entire MCMC samples during an initial transition time are discarded. Hence, after accumulating a sufficient number of samples, the set of realizations of the model parameter $\boldsymbol{\theta}$ will reflect directly the posterior probability distribution $p(\boldsymbol{\theta}|\mathbf{seq},\ M_{\text{cut}})$.

Step 3: In this step, we generate a sequence of events taking place during the target forecasting interval of $[T_{\text{start}}, T_{\text{end}}]$ which is denoted as $\mathbf{seq_g}$ in eq. (3). In order to generate $\mathbf{seq_g}$ given the samples $\boldsymbol{\theta}$, **seq** and M_{cut}, a stochastic procedure is adopted according to Ebrahimian & Jalayer (2017). The procedure is illustrated by a flowchart in Fig. 4. The probability distribution $p(\mathbf{seq_g}|\boldsymbol{\theta}, \mathbf{seq},\ M_{\text{cut}})$ is given by eq. (7) as follows:

$$p\left(\mathbf{seq_g}\,|\boldsymbol{\theta}, \mathbf{seq}, M_{\text{cut}}\right) = \Pi_i\, p(IAT_i, x_i, y_i, M_i|\ \mathbf{seq}_{\mathbf{g}i-1}, \boldsymbol{\theta}, \mathbf{seq},\ M_{\text{cut}}), \tag{7}$$

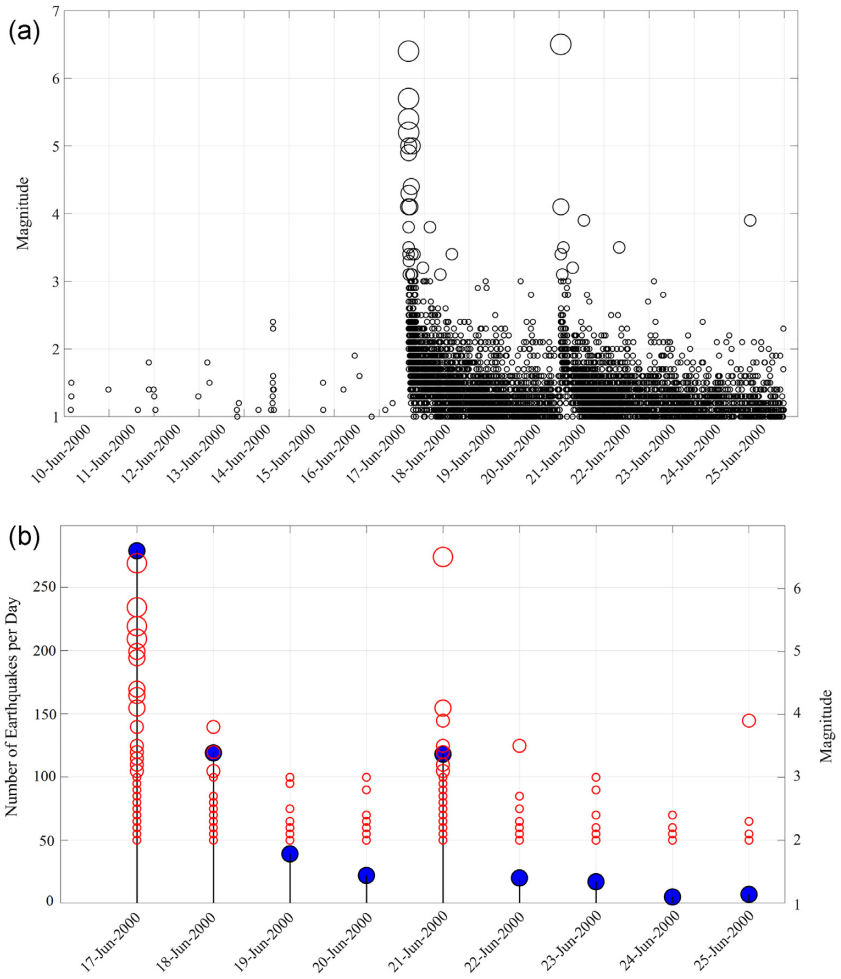

Figure 3. (a) Temporal evolution of the earthquakes with $\boldsymbol{M} \geq 1.0$ during the June 2000 seismic sequence and (b) daily number of earthquakes with $\boldsymbol{M} \geq 2.0$ shown by blue circles (left-side *y*-axis). Distribution of earthquake magnitudes per day shown by red circles (right-side *y*-axis), the diameter of red circles is proportional to $\boldsymbol{M}$.

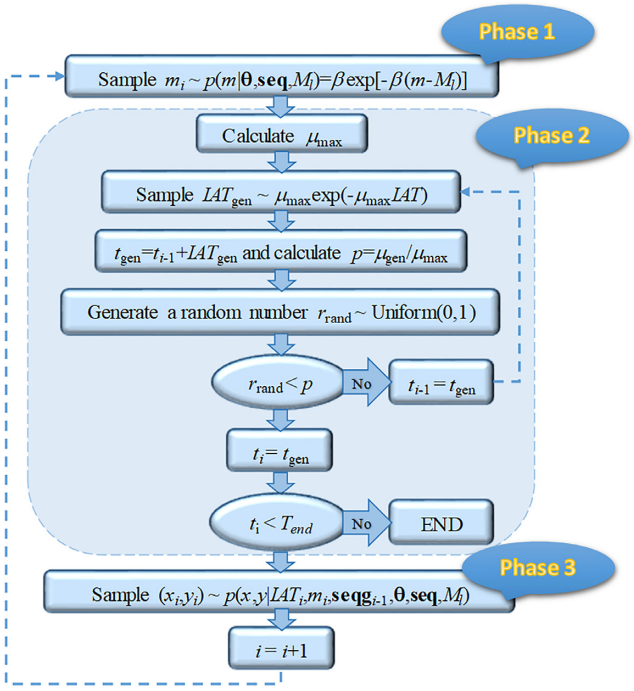

Figure 4. Generating sequences according to $p(\mathbf{seq_g}|\boldsymbol{\theta}, \mathbf{seq}, M_{cut})$ (see fig. S4 in Ebrahimian & Jalayer 2017). The M_l shown in the flowchart is the same as M_{cut} used in this study.

where $\mathbf{seq}_{\mathbf{g}i} = \{\mathbf{seq}_{\mathbf{g}i-1}, (IAT_i, x_i, y_i, m_i)\}$ and $IAT_i = t_i - t_{i-1}$ stands for interarrival time for the ith event and implies the time between two consecutive events. Using the probability product rule, the right-side term can be further expanded as follows:

$$p(IAT_i, x_i, y_i, m_i|\mathbf{seq}_{\mathbf{g}i-1}, \boldsymbol{\theta}, \mathbf{seq}, M_{\text{cut}}) = p(m_i|\mathbf{seq}_{\mathbf{g}i-1}, \boldsymbol{\theta}, \mathbf{seq}, M_{\text{cut}})$$
$$.p(IAT_i|\, m_i, \mathbf{seq}_{\mathbf{g}i-1}, \boldsymbol{\theta}, \mathbf{seq}, M_{\text{cut}})$$
$$.p(x_i, y_i|IAT_i, m_i, \mathbf{seq}_{\mathbf{g}i-1}, \boldsymbol{\theta}, \mathbf{seq}, M_{\text{cut}}) \quad (8)$$

where $p(m_i|\mathbf{seq}_{\mathbf{g}i-1}, \boldsymbol{\theta}, \mathbf{seq}, M_{\text{cut}})$ is the marginal PDF for the magnitude m_i given the earthquake sequence that precede the ith event, $\boldsymbol{\theta}$ and M_{cut}; $p(IAT_i|\, m_i|\mathbf{seq}_{\mathbf{g}i-1}, \boldsymbol{\theta}, \mathbf{seq}, M_{\text{cut}})$ is the conditional marginal PDF for interarrival time given the magnitude is equal to m_i; and finally, $p(x_i, y_i|IAT_i, m_i, \mathbf{seq}_{\mathbf{g}i-1}, \boldsymbol{\theta}, \mathbf{seq}, |M_{\text{cut}})$ is the conditional joint PDF for the spatial centre (x_i, y_i) given that IAT_i and m_i are known. In other words, as shown in Fig. 4, in phase 1, we first generate the m_i within $\mathbf{seq}_{\mathbf{g}}$ according to the truncated Exponential PDF with rate β. Then, in phase 2, given the m_i is already generated in the previous phase, the IAT_i is generated using the Thinning algorithm in which, first, the temporal Poisson rate over the whole aftershock zone is computed (see eq. 9) for an earthquake with m_i and time t_{i-1} (denoted as $\mu_{\max}$). t_{i-1} is associated with the first earthquake that is going to happen in the target forecasting interval (i.e. t_{gen}). Next, IAT_{gen} is generated from a homogeneous Exponential PDF with the form $\mu_{\max}\exp(-\mu_{\max} IAT)$. We note that this term is equivalent to $IAT_{\text{gen}} = \frac{-\log(1-r_{\text{rand}})}{\mu_{\max}}$ and r_{rand} is a random number generated from a Uniform distribution from 0 to 1. By replacing t_{gen} with t_{i-1} in eq. (9), we calculate the Poisson rate at time $t_{\text{gen}} = t_{i-1} + IAT_{\text{gen}}$ (denoted as μ_{gen}). In case IAT_{gen} is accepted with the probability $p = \frac{\mu_{\text{gen}}}{\mu_{\max}}$, the phase 2 continues by producing new IAT_{gen} until it exceeds the T_{end}. If t_{gen} is rejected with probability $1 - p$, a new IAT_{gen} is sampled from the homogeneous Exponential PDF with rate $\mu_{\max}$.

$$\mu_{\max} = \iint_{x,y} \mu_{\text{ETAS}}\,(t_{i-1}, x, y, m_i|\mathbf{seq}_{\mathbf{g}i-1}, \boldsymbol{\theta}, \mathbf{seq}, M_{\text{cut}})\mathrm{d}x\,\mathrm{d}y. \quad (9)$$

Finally, in phase 3, given m_i, t_i and $\mathbf{seq}_{\mathbf{g}i-1}$(the previous events in the generated sequence) are already computed in phase 1 and 2, the coordinates (x_i, y_i) are sampled. Sampling from $p(x_i, y_i|IAT_i, m_i, \mathbf{seq}_{\mathbf{g}i-1}, \boldsymbol{\theta}, \mathbf{seq}, M_{\text{cut}})$ is described in detail in Ebrahimian & Jalayer (2017).

Step 4: Finally, a robust estimate for $N(x, y, m|\mathbf{seq}, M_{\text{cut}})$ is obtained considering the associated uncertainties in the spatio-temporal distribution of the sequence of events according to eq. (3). Various confidence intervals of $N(x, y, m|\mathbf{seq}, M_{\text{cut}})$, namely 2^{nd}, 16^{th}, 50^{th}, 84^{th} and 98^{th} percentiles, as well as the mean estimate are computed for each spatial cell unit and for various magnitude thresholds m. Hence, at this stage, the spatial short-term seismicity forecasting maps can be produced for earthquakes with magnitude equal to or above m including their corresponding uncertainty in each cell.

Step 5: In this step, we sum the $\mathrm{E}[N(x, y, m|\mathbf{seq}, M_{\text{cut}})]$ from eq. (3) over the entire cell units comprising the predefined aftershock zone to obtain $N(m|\mathbf{seq}, M_{\text{cut}})$ (assuming that the integral of the spatial kernel over the aftershock zone is sufficiently close to unity). In this way, we multiply $N(x, y, m|\,\mathbf{seq},\ M_{\text{cut}})$ by the cell unit dimension $\mathrm{d}x\ \mathrm{d}y$ and also the number of cell units (= the whole aftershock zone area). The probability that an event exceeding a given magnitude level m occurs within the aftershock zone in the forecasting interval can be calculated by the exponential distribution as follows (Ebrahimian & Jalayer 2017):

$$Pr\ (M \geq m) = 1 - \exp\left(-N\,(m|\mathbf{seq}, M_{\text{cut}})\right) = 1 - \exp\left(\int\int_{x,y\in A} -\mathrm{E}\left[N\,(x, y, m|\mathbf{seq}, M_{\text{cut}})\right]\mathrm{d}x\,\mathrm{d}y\right). \quad (10)$$

The inference of the ETAS parameters is adaptively updated, that is the posteriors of the ETAS parameters obtained from the previous forecasting interval can be used as priors for the subsequent forecasting interval.

4. SHORT-TERM SEISMICITY FORECASTING RESULTS AND DISCUSSION

To appraise the forecasting skill of the calibrated model we attempt to replicate the progression of the June 2000 seismic sequence after the 17 June main shock over short-term forecasting intervals of various durations and starting times, both in terms of the expected number of events and their spatial distribution in a defined aftershock region. This region is a zone that at minimum covers the geographical distribution of the 2000 seismic sequence and here it is chosen as the entire SISZ and RPOR (see Fig. 2). For the purpose of spatial forecasting of sufficient resolution, the aftershock zone is gridded into square approximately 1 km^2 cells (0.0227° longitude × 0.01° latitude). The short-term seismicity rates for various magnitudes are estimated spatially for each grid cell. We note that the grid resolution is much higher than in the previous study by Eberhard (2014).

We issue short-term spatio-temporal seismicity forecasts for aftershocks of magnitudes M_{cut} and larger over intervals with different start times (T_{start}) after the main shocks and with durations (i.e. T_{end}—T_{start}) ranging from 4 to 24 hr. The forecasted total number of events, their spatial distribution and cumulative probabilities of earthquake occurrence by magnitude are reported for the defined aftershock zone. The lower cut-off magnitude, M_{cut}, is calculated using two methods explained in Section 4.1. Hence, **seq** (in eq. 3) is constructed by segregating events with $M \geq M_{\text{cut}}$ that occurred during $[T_0,\ T_{\text{start}})$ in the aftershock zone. Then, the Bayesian spatio-temporal ETAS model is applied to the assembled **seq** available at the time of issuing forecast. In this regard, the first step is to sample values of $\boldsymbol{\theta}$ which are generated as a

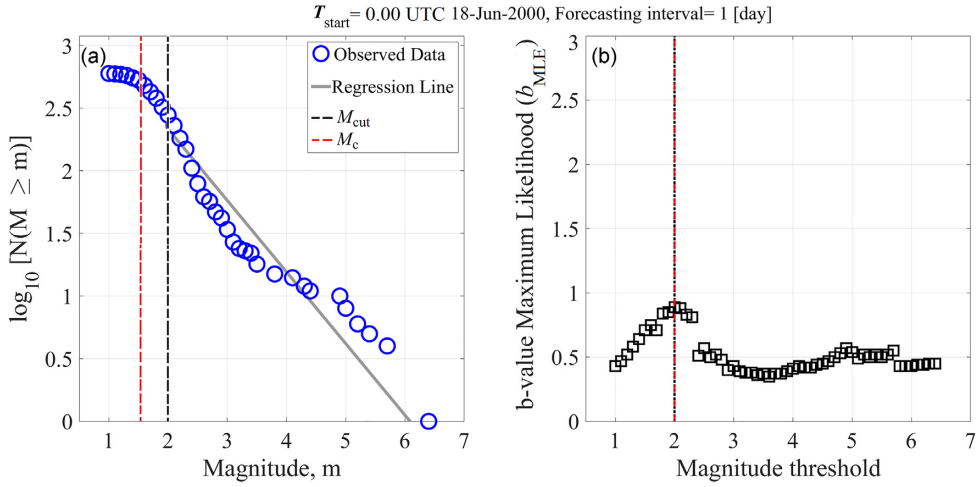

Figure 5. Magnitude of completeness calculation for 24-hr forecasting interval of 18 June 2000 using two methods conventional fitting (left-hand panel) and Bayesian updating approach proposed by Ebrahimian *et al.* (2014) (right-hand panel). The black dotted lines and red dashed lines show lower cut-off magnitude ($\boldsymbol{M_{cut}}$) and magnitude of completeness ($\boldsymbol{M_c}$), respectively. The observed data points are plotted by blue circles and the maximum likelihood estimates for the posterior probability distribution of $\boldsymbol{b}$-value ($\boldsymbol{b_{MLE}}$) are depicted by black squares.

Markov Chain sequence from the posterior distribution of the ETAS model parameters, $p(\boldsymbol{\theta}|\mathbf{seq},\ M_{cut})$, conditional on the M_{cut} and **seq**. The MCMC samples of the ETAS parameters presented in this section are drawn from 220 iterations within the last simulation level considering five consecutive simulation levels, which was found to be sufficient in terms of reliability of results and efficiency of simulations, in particular for a potential OEF system for Iceland. To reach this, we thoroughly appraised the impact of number of MCMC samples of posterior PDF $p(\boldsymbol{\theta}|\mathbf{seq},\ M_{cut})$ on the uncertainty of ETAS parameters, and consequently on the resultant seismicity forecasts based on detail convergence diagnostic analyses (for detail, see Supporting Information S1). In the next step, $\mathbf{seq_g}$—simulated events that are going to take place during the forecasting interval—is generated from the PDF $p(\mathbf{seq_g}|\boldsymbol{\theta}, \mathbf{seq},\ M_{cut})$ for the given samples of $\boldsymbol{\theta}$ (see Ebrahimian & Jalayer 2017, for more details). It is worth noting that the effect of background seismicity is ignored in this work due to the low seismicity level prior to the sequence (see Fig. 3). The resulting forecasted maps are shown in Sections 4.2 and 4.3.

4.1 Magnitude of completeness

The completeness of the seismic sequence, the progression of which is to be forecasted, requires the prior estimation of its magnitude of completeness (M_c) before applying the Bayesian ETAS model. Strictly speaking, M_c should be estimated for each subsequent earthquake catalogue registered at the time of issuing the forecast. The estimated M_c is considered as a lower magnitude-bound of seismic sequences and hence the desired lower cut-off magnitude, M_{cut} (see eqs 1–3) in subsequent forecasting intervals should be set greater than or equal to M_c.

We adopted two approaches to evaluate M_c: (i) conventional linear regression analysis and (ii) the Bayesian b-value estimation method (see Ebrahimian *et al.* 2014, 2019). The first approach is based on linear regression over the conventional magnitude-frequency distribution of observed (registered) events occurred during $[T_0, T_{start})$. This procedure is a well-established and widely used method which is most effective owing to the fact that our database includes a large number of small events ($M < 4.0$) and only a few numbers of medium-to-large magnitude events (see Fig. 3).

In this procedure, the Gutenberg–Richter relationship is applied by fitting a linear relation to the logarithmic frequency versus magnitude distribution $\log_{10}[N(M \geq m)] = a - bm$ of the events within $[T_0, T_{start})$ corresponding to the desired forecasting interval. The parameters a and b are the coefficients of linear regression, and M_c is identified as the starting point of the linear attribute of $\log[N(M \geq m)]$ versus m data points. The second approach is based on Bayesian updating of the b-value against a set of magnitude thresholds. In this procedure, M_c is defined by visual inspection of the stability (invariability) of the maximum likelihood estimates (b_{MLE}) for the posterior probability distribution of b. The magnitude threshold at which b_{MLE} becomes roughly invariant represents the corresponding M_c for the desired forecasting interval. This method is similar to the b-value stability approach proposed by Cao & Gao (2002). For further explanation see Supporting Information.

We obtained M_c for various subcatalogues associated with different short-term forecasting intervals evaluated in this work. For all forecasting analyses, the M_c calculation is performed automatically. For instance, Fig. 5 shows the M_c calculation for the 24-hr forecasting time interval with T_{start}= 00:00 UTC of 18 June 2000 (all times UTC hereafter). The Fig. 5(a) displays $\log[N(M \geq m)]$ versus magnitude m distribution of the observed events with $M \geq 1.0$ (blue circles) that occurred during $[T_0, T_{start})$, where T_0 = 15:40 on 17 June 2000. The grey line is the linear regression model. $M_c = 1.6$ is the lowest magnitude above which $\log[N(M \geq m)]$ versus m becomes linear, as indicated with a red dashed line in Fig. 5.

The Fig. 5(b) illustrates the application of the second method, where b_{MLE} is plotted against various magnitude thresholds. The magnitude threshold at which the increasing trend in b_{MLE} is stopped is $M_c = 2.0$ (see the red dashed line). This figure reveals that b-value is not constant but depends on a lower magnitude threshold. In this regard, Godano *et al.* (2014) observed three regimes: (1) Increasing b-value for $M < M_c$

which is attributed to catalogue incompleteness where many events are not recorded, (2) a magnitude interval where the b-value is a decreasing function of threshold magnitude, followed by (3) a subsequent slight increase for large magnitudes. Fig. 5(b) illustrates similar attributes for the June 2000 earthquake sequence for the 18 June forecasting interval. Furthermore, similar trends have been observed for the subsequent forecasting intervals during the June 2000 sequence.

To comply with $M_{\rm cut} \geq M_{\rm c}$ while considering the time-consuming computational demand, the larger $M_{\rm c}$ is chosen as $M_{\rm cut}$ for forecasting analyses (i.e. $M_{\rm cut} = 2.0$) and depicted by black dashed lines in Fig. 5. Similar observation was provided for the proceeding short-term forecasting intervals and therefore, $M_{\rm cut}$= 2.0 is used for almost all the forecasting intervals studied herein. In general, due to lack of data in the early aftershock period, the $M_{\rm c}$ for the earlier forecasting intervals immediately after a main shock tends to be higher than the estimated value for later forecasting intervals when more data is available. However, in this study, the incompleteness of the seismic catalogue for early forecasts is not problematic because of the Bayesian inference enables training the ETAS model parameters during a seismic sequence through the adaptive learning process of ETAS parameters (even in the presence of small number of registered events).

4.2 Forecasting the aftershock sequence of the 17 June 2000 earthquake

The June 2000 seismic sequence started with a $M_{\rm w}$ 6.4 main shock on 17 June 2000 at 15:40:41 (= T_0). The first seismicity forecast was defined with $T_{\rm start}$ = 19:00 and $T_{\rm end}$ = 24:00 of 17 June (i.e. approximately 3:20′ after the main shock with a forecasting interval of 5 hr). The delay is not a specific number, but we estimate it to realistically reflect the actual delay in preparing the catalogue of recently recorded aftershocks and triggered events immediately following the onset of an intense seismic sequence. This would include, for example manually checking the automatic earthquake locations of the SIL system to ensure the reliability of the catalogue for the Bayesian ETAS forecasting from the main shock until the start time of the forecasting interval, that is [T_0, $T_{\rm start}$), the calculation of $M_{\rm cut}$ (which in this case was equal to 2.0) preparation of the subcatalogue with $M \geq M_{\rm cut}$ as **seq**. The Bayesian ETAS method is subsequently applied and the forecasted number of events in the aftershock zone, $N(x,\ y,\ m|\mathbf{seq},\ M_{\rm cut})$ in eq. (3), is estimated for each 1 km^2 spatial cell units in the region.

For the main five ETAS parameters, that is β, c, p, d and q, an informative prior distribution is desired. As this is model dependent and these parameters have not been estimated before for any sequence in Iceland, we selected the priors based on a thorough literature review (Seif *et al.* 2017; Hardebeck *et al.* 2019; Shcherbakov *et al.* 2019) from other studies done in relatively similar tectonic environments around the world. We note that the selected parameter values have been adjusted to account for potential differences, in particular, in terms of the functional form. Thus, for each of the main ETAS parameters, normal priors with the following mean values of the generic parameters are assumed: $\beta = 1.25$, $c = 0.005$, $d = 1.0$, $q = 1.5$ and $p = 1.5$, all with a constant and sufficiently large value of the coefficient of variation (CV = 0.3) to create prior distributions that cover the range of reasonable values (see first column of Table 1). It should be highlighted that in this study, normal distribution for prior and lognormal distribution for proposal have been exploited for Bayesian prediction. This is also consistent with Shcherbakov *et al.* (2019) demonstrating statistically equivalent Bayesian predictive distribution for different combination of the prior and proposal distributions except for flat priors.

We have also explored the use of ETAS parameters estimates obtained from the previous study for Iceland conducted by Eberhard (2014) as priors in Section 4.5. It should be noted that in our forecasting analysis, in particular, to forecast aftershocks following the first main shock, the effect of background seismicity is negligible compared to the increased seismicity rate following the first main shock on 17 June ($M_{\rm w}$ 6.4). This can be attributed to the rapid decay of seismicity observed in previous sequences with available data (see Fig. 3a). Therefore, including it into the forecasting process had no effect, and as a result we assumed $N_{\rm b}(x, y, m|\ M_{\rm cut})$ to be equal to zero in calculations. For all forecasting intervals, the mean, CV and 95 per cent confidence interval (CI) associated with the posterior distribution of the eight spatio-temporal ETAS model parameters are listed in Table 1 all being associated with well-behaved unimodal and symmetric posterior distributions.

Fig. 6(a) shows the corresponding geographical distribution of the 98th percentile of the forecasted seismicity having $M \geq M_{\rm cut} = 2$, corresponding to $T_{\rm start}$= 19:00 UTC and forecasting interval duration of 5 hr. Presented as a heat map, the likely locations of the forecasted events are represented by progressively intense colourmap. The distribution of the forecasted number of events with $M \geq 2$ in the aftershock zone is given by a median value (in a grey box) along with bars indicating different percentiles: 16$^{\rm th}$ and 84$^{\rm th}$ percentiles (blue numbers) and 2$^{\rm nd}$ and 98$^{\rm th}$ percentiles (black numbers). The percentiles are compared to the actual number of observed earthquakes with $M \geq M_{\rm cut}$ that occurred during the forecasting interval within the aftershock zone is shown by the red star. The spatial locations of these aftershocks and triggered events are given by symbols on the map. Finally, the probabilities of at least one earthquake with a magnitude greater than or equal to 3.5, 4.5, 5.5 and 6.5, respectively, are denoted as $Pr(M \geq m)$ (see eq. 10). The geographical location of the forecasted seismicity is seen to be very consistent with the actual occurrence of aftershocks and triggered seismicity (symbols) during the first 5-hr forecasting interval starting at 19:00 UTC. This is also the case for other forecasting intervals of different start times and durations shown in Fig. 6 (and discussed below), indicating the strong spatial forecasting ability of the forecasting framework only few hours after the main shock.

However, we note that the forecasted number of events considerably overpredicts the number of observed earthquakes $N_{\rm obs} = 67$, which is approximately the level at which the 2nd percentile of the forecasted number is. It is worth noting that the few numbers of moderate magnitude events including three $M_{\rm w}$ 5.7 earthquakes are included in **seq** as they occurred few minutes after the first main shock. Therefore, we investigate the effect of having more data on the forecasting ability of the framework by providing a new seismicity forecast that starts one hour after the first one, that is $T_{\rm start}$= 20:00, for a 4-hr forecasting interval (see Fig. 6b). The resulting ETAS model parameter estimates (mean and CV) have been updated based on progressively richer seismic observed data (i.e. **seq**), and listed in the 3$^{\rm rd}$ column of Table 1.

Table 1. Statistics (mean, coefficient of variation, CV and 95 per cent confidence interval, CI) of Prior and marginal posterior distribution of ETAS parameters for forecasting aftershocks of the 17 June earthquake (M_w 6.4). The forecasting intervals correspond to Figs 5 and 6 maps. The forecasting intervals' duration and T_{start} are reported in the header of each column.

ETAS parameters		Prior	5 hr	4 hr			24 hr		
			19:00 UTC 17-June	20:00 UTC 17-June	20:00 UTC 17-June∗	0:00 UTC 18-June	0:00 UTC 19-June∗∗	0:00 UTC 20-June	0:00 UTC 21-June
β	Mean	1.25	0.895	0.933	0.851	0.985	1.029	1.05	1.062
	CV	0.3	0.047	0.042	0.033	0.034	0.021	0.016	0.013
	95% CI		[0.817,0.972]	[0.862,1.025]	[0.792,0.910]	[0.923,1.045]	[0.987,1.068]	[1.019,1.084]	[1.034,1.090]
c	Mean	0.005	0.005	0.005	0.0057	0.005	0.005	0.005	0.005
	CV	0.3	0.262	0.218	0.192	0.236	0.161	0.109	0.101
	95% CI		[0.003,0.007]	[0.003,0.007]	[0.004,0.008]	[0.003,0.007]	[0.004,0.007]	[0.004,0.006]	[0.004,0.006]
p	Mean	1.5	1.113	1.152	1.117	1.234	1.21	1.204	1.201
	CV	0.3	0.076	0.079	0.070	0.057	0.028	0.024	0.019
	95% CI		[1.004,1.276]	[1.010,1.382]	[1.007,1.251]	[1.065,1.337]	[1.145,1.268]	[1.145,1.256]	[1.153,1.241]
d	Mean	1	1.039	1.100	1.031	1.014	0.859	0.829	0.81
	CV	0.3	0.148	0.102	0.127	0.112	0.086	0.061	0.046
	95% CI		[0.815,1.314]	[0.915,1.310]	[0.817,1.257]	[0.848,1.311]	[0.696,0.999]	[0.745,0.914]	[0.733,0.878]
q	Mean	1.5	1.563	1.598	1.605	1.581	1.605	1.602	1.604
	CV	0.3	0.045	0.033	0.036	0.036	0.021	0.017	0.014
	95% CI		[1.446,1.676]	[1.513,1.700]	[1.507,1.717]	[1.502,1.751]	[1.533,1.680]	[1.554,1.652]	[1.561,1.648]
K	Mean		7.743	1.726	3.143	0.699	0.609	0.59	0.576
	CV		4.508	1.439	1.774	0.475	0.093	0.082	0.061
	95% CI		[0.724,32.521]	[0.553,10.137]	[0.674,15.354]	[0.502,1.524]	[0.516,0.733]	[0.515,0.700]	[0.516,0.659]
K_t	mean		0.048	0.058	0.053	0.065	0.068	0.069	0.069
	CV		0.496	0.269	0.386	0.115	0.033	0.025	0.021
	95% CI		[0.004,0.073]	[0.010,0.072]	[0.006,0.076]	[0.046,0.074]	[0.064,0.073]	[0.065,0.072]	[0.066,0.072]
K_R	Mean		0.194	0.217	0.205	0.192	0.161	0.154	0.149
	CV		0.289	0.208	0.255	0.247	0.136	0.098	0.069
	95% CI		[0.120,0.302]	[0.157,0.315]	[0.134,0.317]	[0.141,0.360]	[0.120,0.209]	[0.128,0.181]	[0.130,0.170]

∗For all forecasting scenarios, the $M_{cut} = 2.0$, except this forecasting analysis in which M_{cut} is set to 1.5.
∗∗After this forecasting interval, the mean and CVs of the posteriors from the preceding interval are used as priors for the subsequent one.

The same prior values as the previous forecasting analysis (i.e. first column of Table 1) are used. The Fig. 6 (b) exhibits the corresponding seismicity forecasting map in terms of the 98th percentile of the estimated number of earthquakes with $M \geq 2.0$. We note that compared to the first forecasting interval that started 1-hr earlier (see Fig. 6a), $Pr(M \geq 6.5)$ decrease by about 25 per cent, that is as more time passes, the probability of experiencing another strong earthquake decreases. Still, the same relative overprediction of the forecasted number of events (their 2nd percentile is 42) is obtained versus the observed ($N_{obs} = 41$).

To further examine the impact of larger dataset available to the Bayesian ETAS forecasting over the admittedly relatively short forecasting interval, we manually pick a lower M_{cut} value of 1.5, in spite of the estimated M_{cut} value of 2.0 and run forecasting analysis again for the same 4-hr forecasting interval with T_{start}= 20:00, but now for a richer seismic catalogue of **seq**. The results are shown in Fig. 6(c). This time the forecasting performs much better with the estimated distribution of the number of events of $M \geq 1.5$ (boxplot showing the forecasted number of events with median of 151 (16–84th percentile interval is 126–176) being remarkably consistent with the observed number of events ($N_{obs} = 131$). Thus, when issuing forecasts in the immediate aftermath of the 17 June earthquake, the quantity of smaller events has a significant impact on the accuracy of the forecasted seismicity. We also note that now the exceedance probabilities of forecasted earthquakes larger than 5.5 and 6.5 are back at high values. However, no events larger than magnitude 4 occurred over the (admittedly) short forecasting interval.

We expand the forecasting intervals from few hours to daily forecasts for the subsequent days of 18 June to 21 June with the arbitrary starting times of midnight (T_{start}= 00:00), the first one being for the entire 24 hr of 18 June 2000. The same ETAS model parameters as in the immediate forecasts are used as priors for the first daily forecast with their prior mean and CV listed in the first column of Table 1. During each forecasting interval, the ETAS model parameters are adaptively updated with new posteriors, that in turn serve as priors for the next forecasting interval (i.e. the next day). The posterior statistics (mean, CV and 95 per cent CI) of all parameters computed for all forecasting intervals are listed in subsequent columns of Table 1. The results are presented in map format in Fig. 7. They show that for the daily forecasts from 18 to 20 June 2000, the observed number of events with $M \geq M_{cut} = 2$ are very well predicted by the robust forecasting framework lying in the range of 16th to 84th percentiles of the forecasted number of events.

The exception however is, as expected, the daily forecast for 21 June as it severely underpredicts the total number of observed events ($N_{obs} = 118$), mainly due to the fact that M_w 6.5 (at 00:51 UTC on 21 June) was not preceded by any notable increase in the seismicity. Also, the forecast assigned only a 15 per cent probability of an earthquake larger than M_w5.5 occurring on 21 June according (Fig. 7). The forecasting interval starting 51 min before the second main shock essentially rendered it useless as fundamental assumptions had changed.

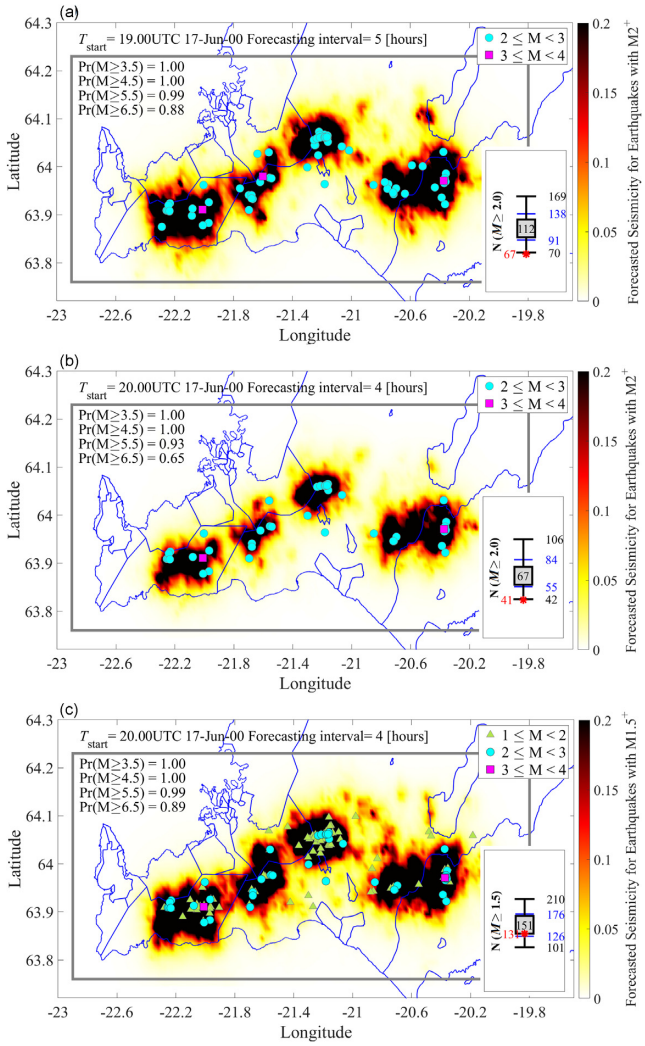

Figure 6. Early seismicity forecasting maps for earthquakes with $\boldsymbol{M \geq M_{cut}}$ across the aftershock zone following the 17 June 2000 main shock at 15:40 UTC ($\boldsymbol{M_w}$6.4). The aftershock zone includes the SISZ and RPOR in SW-Iceland and outlined by the grey lines in the maps. The starting time and duration of the forecasting time interval corresponding to each seismicity forecasting map are reported on the top of each panel. The observed earthquakes with $\boldsymbol{M \geq M_{cut}}$ occurred during the target forecasting interval are depicted by different symbols w.r.t their corresponding $\boldsymbol{M}$. $\boldsymbol{Pr(M \geq m)}$, $\boldsymbol{m}$ = 3.5, 4.5, 5.5 **and** 6.5, listed on the top left-hand corner of each map, represent the probabilities of having at least one earthquake exceeding the defined magnitude threshold across the aftershock zone in the forecasting interval. The right-hand side error-bar illustrates the forecasted number of earthquakes with $\boldsymbol{M \geq M_{cut}}$ for the whole SW-Iceland for the interval: the median value (50th percentile) is reported within the grey-filled square and the blue numbers present the 16th and 84th percentiles and the black numbers indicate the 2nd and 98th percentiles. The number of actual observed earthquakes with $\boldsymbol{M \geq M_{cut}}$ occurred during the forecasting interval within the aftershock zone is shown by a red star. We note that for the first two forecasts, the $\boldsymbol{M_{cut}}$ is equal to 2.0, while for the last early forecasting map, the $\boldsymbol{M_{cut}}$ is assumed 1.5, thereby the forecasted and observed seismicity distributions are presented for $\boldsymbol{M \geq 1.5}$.

It is thus a clear indicator that an operational earthquake forecasting framework needs to use an adaptive approach to assign forecasting intervals, essentially resetting when there is a significant change in the seismicity that was not forecasted by the preceding sequence, for example the occurrence of a main shock event.

4.3 Forecasting the aftershock sequence of the 21 June 2000 earthquake

The M_w 6.5 earthquake on 21 June at 00:51 struck the central part of the SISZ on a different fault than the 17 June earthquake. It therefore marks the beginning of a new seismic sequence as shown in Fig. 3, confirmed also by the rapid decay of seismicity of the previous sequence. We therefore adjust our forecasting time intervals to start shortly after the second main shock, in a similar manner as for the first one. The two forecasting intervals considered are (1) a 20-hr forecasting interval starting at 4:00 am UTC, approximately 3 hr after the main shock, (see Fig. 8a) and (2) an 18-hr forecasting interval starting at 6:00 am, both ending at 24:00 of 21 June 2000 (see Fig. 8b). In the same way as before, the corresponding seismicity forecasts for aftershocks with $M \geq M_{cut}$ (= 2.0) over the aftershock zone are shown in Fig. 8. The box plot and error-bars show the good agreement between the forecasted number of events with $M \geq 2.0$ for both early forecasting periods and the observed number of aftershocks (red star). Table 2 lists the corresponding mean, CVs and 95 per cent CI of the posterior distributions

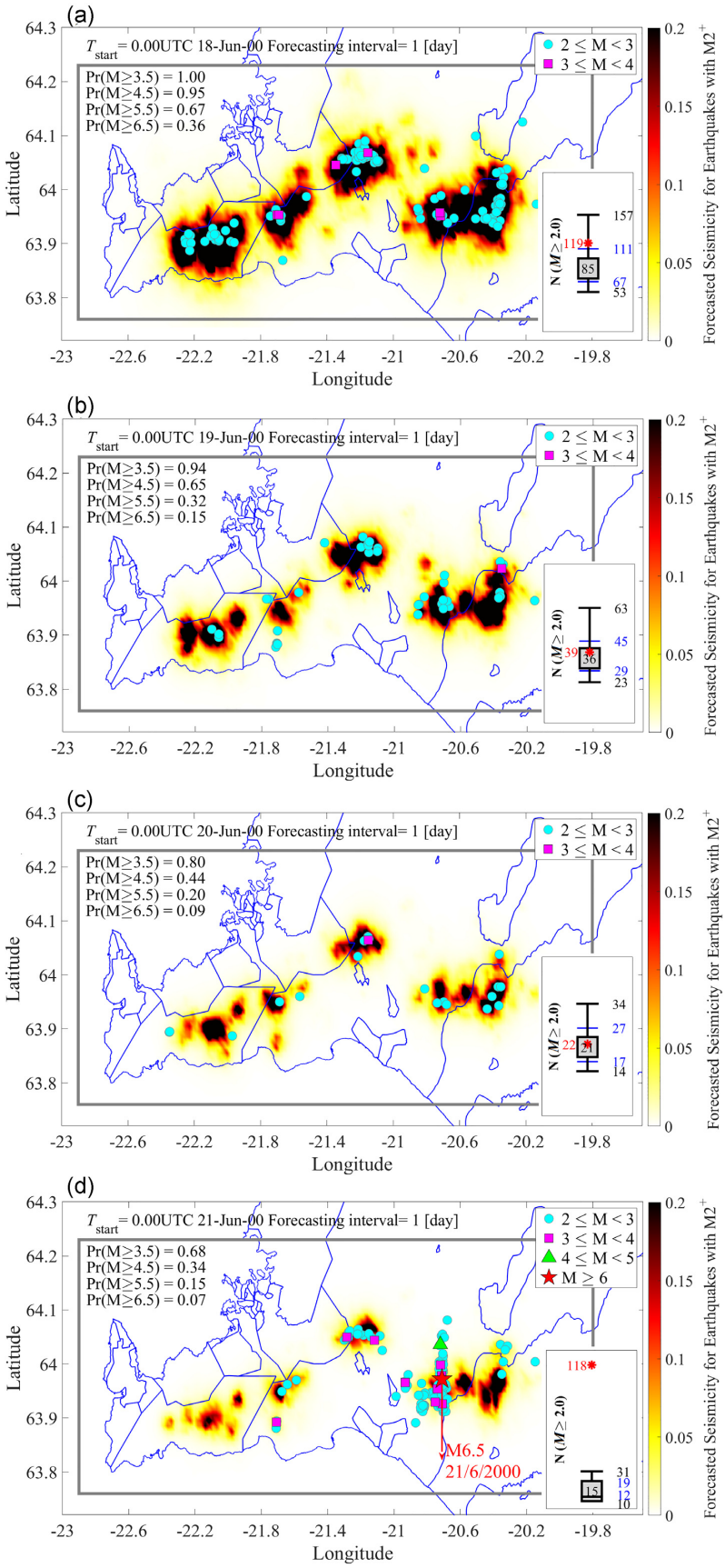

Figure 7. Daily seismicity forecasting maps for earthquakes with $M \geq 2.0$ (denoted as $M2^{+}$ in the colour bar label) across the aftershock zone following the 17 June 2000 main shock at 15:40 UTC (M_w6.4). See the caption to Fig. 6 for more information.

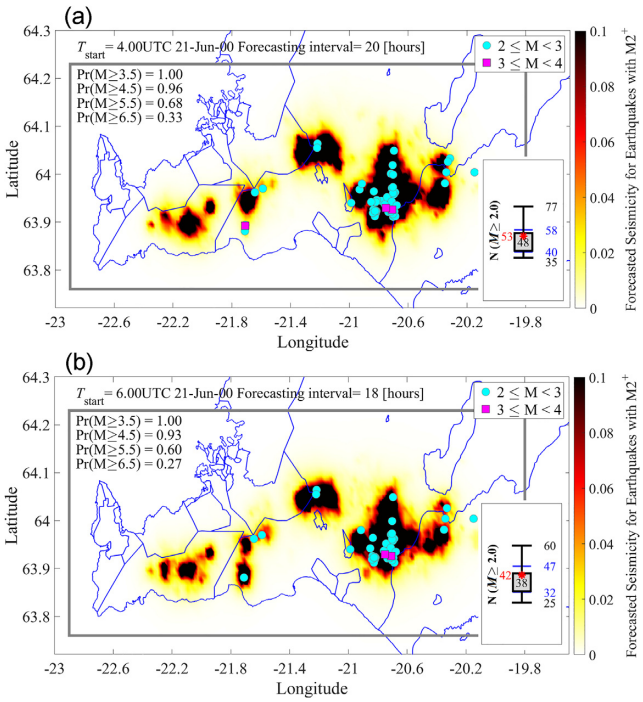

Figure 8. Early seismicity forecasting maps for earthquakes with $M \geq 2.0$ (denoted as $M2^+$ in the colour bar label) across the aftershock zone following the 21 June 2000 main shock at 00:51 UTC (M_w6.5). The aftershock zone includes the SISZ and RPOR in SW-Iceland and outlined by the grey lines in the maps. The starting time and duration of the forecasting time interval corresponding to each seismicity forecasting map are reported on the top of each panel. The observed earthquakes with $M \geq 2.0$ occurred during the target forecasting interval are depicted by different symbols w.r.t their corresponding M. $Pr(M \geq m)$, $m = 3.5, 4.5, 5.5$ and 6.5, listed on the top left corner of each map, represent the probabilities of having at least one earthquake exceeding the defined magnitude threshold across the aftershock zone. The right-hand side error-bar illustrates the estimated number of earthquakes with $M \geq 2.0$ for the whole SW-Iceland corresponding to the forecasting interval: the median value (50th percentile) is reported within the grey-filled square and the blue numbers present the 16th and 84th percentiles and the black numbers indicate the 2nd and 98th percentiles. The number of observed earthquakes with $M \geq 2.0$ occurred during the forecasting interval within the aftershock zone is shown by a red star.

of the ETAS model parameters. We note that the priors for the key ETAS parameters for these first forecasting intervals are also listed, being initially the same ones as for the first sequence (see Table 1). We also note that **seq** starts from the first main shock ($=T_0$) until the start time of the above forecasting intervals.

Both early forecasts show that the observed number of events lies within the 16–84th percentile range of the forecasted number of events. Similarly, the spatial distribution of the seismicity forecast in the aftershock zone is consistent with the actual aftershock occurrence while also impacted by the elevated seismicity areas associated with the first sequence following the first main shock (see the leftmost dark areas in RPOR).

Daily seismicity forecasts for the second sequence were then generated for T_{start} = 6:00 on 21 June and then again at T_{start} = 6:00 on 22 June (using the priors starting from the last forecast). The corresponding forecasts are shown in Fig. 9. Both forecasts show excellent performance with the median of 45 and 22, effectively matching the observed number of events of with $M \geq 2.0$ equal to 48 and 22, respectively. In SISZ, the epicentral locations of the actual events are in great agreement with the forecast expectations while over western RPOR, the forecasted dark area which is mainly influenced by the strong cluster of aftershocks occurred following the first main shock up to 19 June 2000 is not quite consistent with observation. Essentially repeating the forecasts but now for the 22nd, 23rd and 24th of June with start time at midnight (T_{start}= 0:00), the forecasted number of events matches well the observed number of events, apart from 24th of June where the model overpredicts considerably the number of evens (not shown). Further forecasts were not made due to the rapid decay of seismicity with time and few if any events larger than M_{cut} = 2.0.

Compared to the second sequence, higher seismicity, that is in terms of number of events, was forecasted couple of hours after the first main shock while both main shocks have almost similar M_w. The reason is the significantly larger and intense number of observed events that was registered immediately following the 17 June large earthquake, in particular considering aftershocks with moderate-to-large M_w (see Fig. 3).

4.4 The ETAS model parameters' posterior distributions

The posterior mean, CV and 95 per cent CI of the ETAS model parameters in Tables 1 and 2 were obtained from MCMC simulations for various short-term forecasting intervals following the two large earthquake of 17 and 21 June 2000, respectively. The mean and CV of

Table 2. Statistics (mean, coefficient of variation, CV, and 95 per cent CI) of prior and marginal posterior distribution of ETAS parameters for forecasting aftershocks of the 21 June earthquake (M_w 6.5). The forecasting intervals correspond Figs 8 and 9 maps. The forecasting intervals' duration and T_{start} are reported in the header of each column. Note that the **seq** starts from the origin time of the 17 June earthquake occurrence.

ETAS parameters		Priors	20 hr 4:00 UTC 21-June	18 hr 6:00 UTC 21-June	6:00 UTC 21-June	∗6:00 UTC 22-June	24 hr ∗∗0:00 UTC 22-June	0:00 UTC 23-June	0:00 UTC 24-June
β	Mean	1.25	1.09	1.085	1.089	1.09	1.069	1.075	1.08
	CV	0.3	0.025	0.024	0.027	0.018	0.012	0.009	0.007
	95% CI		[1.038,1.147]	[1.027,1.142]	[1.036,1.152]	[1.053,1.126]	[1.046,1.093]	[1.056,1.093]	[1.064,1.096]
c	Mean	0.005	0.0033	0.0036	0.0037	0.0036	0.005	0.005	0.005
	CV	0.3	0.208	0.250	0.258	0.186	0.092	0.095	0.095
	95% CI		[0.002,0.005]	[0.002,0.006]	[0.002,0.006]	[0.002,0.005]	[0.004,0.006]	[0.004,0.006]	[0.004,0.005]
p	Mean	1.5	1.139	1.156	1.156	1.157	1.199	1.197	1.197
	CV	0.3	0.027	0.035	0.033	0.019	0.015	0.012	0.011
	95% CI		[1.079,1.199]	[1.090,1.243]	[1.090,1.223]	[1.115,1.204]	[1.161,1.230]	[1.171,1.224]	[1.175,1.227]
d	Mean	1	0.783	0.724	0.777	0.766	0.798	0.793	0.784
	CV	0.3	0.075	0.106	0.081	0.057	0.039	0.037	0.029
	95% CI		[0.675,0.880]	[0.595,0.840]	[0.645,0.891]	[0.675,0.853]	[0.736,0.853]	[0.736,0.851]	[0.742,0.827]
q	Mean	1.5	1.582	1.551	1.581	1.584	1.603	1.602	1.604
	CV	0.3	0.027	0.032	0.025	0.017	0.013	0.011	0.01
	95% CI		[1.502,1.658]	[1.486,1.639]	[1.517,1.643]	[1.528,1.639]	[1.557,1.641]	[1.562,1.635]	[1.570,1.633]
K	Mean		0.662	0.636	0.627	0.602	0.564	0.553	0.544
	CV		0.139	0.164	0.155	0.084	0.048	0.038	0.032
	95% CI		[0.527,0.894]	[0.485,0.869]	[0.496,0.879]	[0.513,0.711]	[0.514,0.622]	[0.518,0.596]	[0.508,0.579]
K_t	Mean		0.062	0.063	0.063	0.064	0.069	0.068	0.068
	CV		0.075	0.082	0.082	0.044	0.018	0.019	0.018
	95% CI		[0.049,0.068]	[0.052,0.070]	[0.051,0.071]	[0.058,0.069]	[0.067,0.072]	[0.066,0.071]	[0.065,0.070]
K_R	Mean		0.140	0.125	0.139	0.136	0.146	0.145	0.143
	CV		0.129	0.170	0.133	0.088	0.064	0.057	0.043
	95% CI		[0.110,0.172]	[0.093,0.163]	[0.106,0.171]	[0.114,0.164]	[0.130,0.164]	[0.129,0.161]	[0.131,0.155]

∗The priors for this forecasting interval are the mean and CV of the marginal posteriors from the previous one

∗∗The priors for this forecasting interval are those in the last column of Table 1. Then, after this forecasting interval, the mean and CVs of the marginal posteriors from the preceding interval are used as priors for the subsequent one

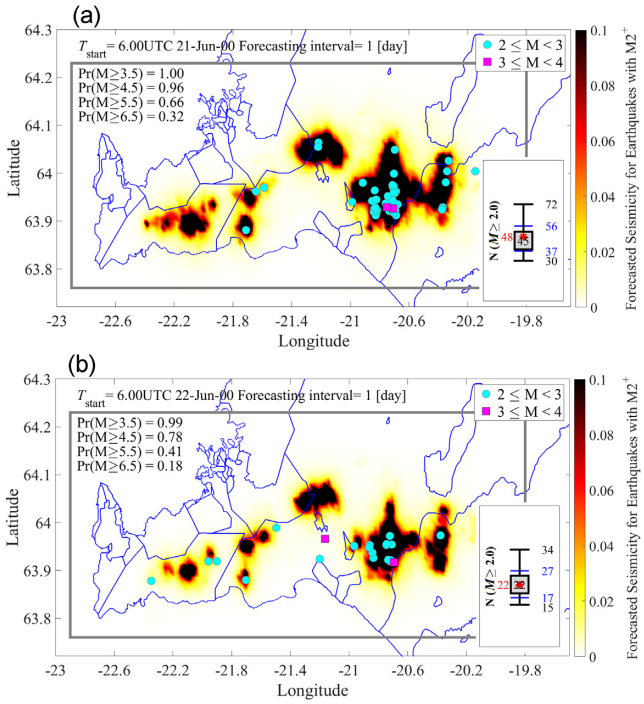

Figure 9. Daily spatio-temporal seismicity forecasting maps for earthquakes with $M \geq 2.0$ (denoted as $M2^+$ in the colour bar label) across the aftershock zone following the 21 June 2000 main shock at 00:51 UTC (M_w 6.5). See the caption to Fig. 8 for more information.

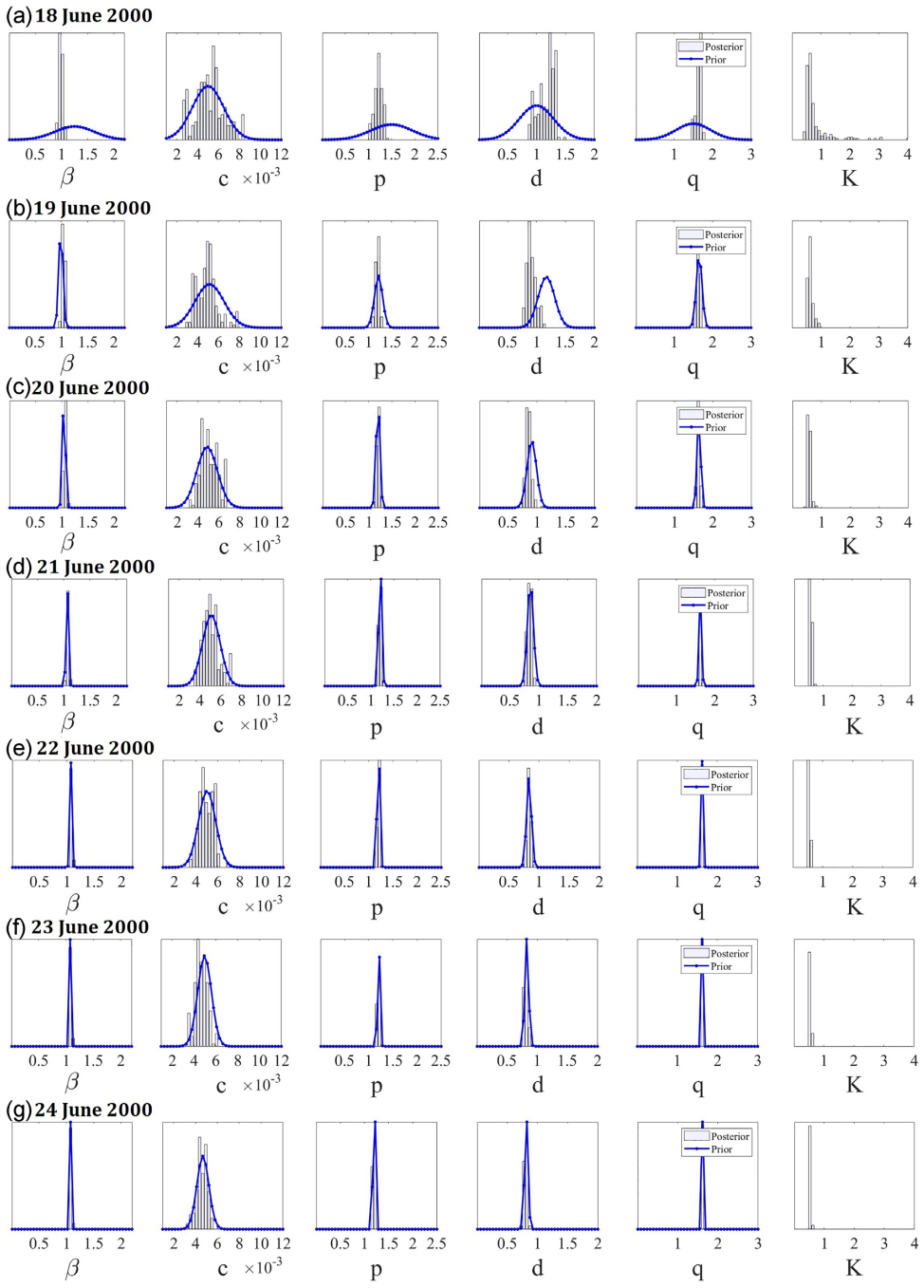

Figure 10. Marginal posterior probability distributions of six ETAS parameters (i.e. $[\beta,\ c,\ p,\ d,\ q,\ K]$) used for daily seismicity forecasting along with the daily updated prior distributions (blue curves) for seven 24-hr forecasting intervals with $T_{\text{start}} = 0{:}00$ UTC from 18 June up to 24 June 2000.

the marginal posterior distributions of the ETAS model parameters from the previous forecasting interval were used as priors for the next forecasting interval while providing the daily seismicity forecasts for the period 18–24 June with each interval starting at midnight (see Tables 1 and 2 when this operation was undergone for each sequence).

For each daily forecasting interval with $T_{\text{start}} = 0{:}00$ UTC, Fig. 10 shows the corresponding normal distributions used as priors (blue curves) for the six ETAS parameters, $\boldsymbol{\theta} = [\beta,\ c,\ p,\ d,\ q,\ K]$ along with the resulting marginal posterior probability mass function of the Markov chains (grey bar plots). We note that the blue curve (prior) for a subsequent day corresponds to the posterior histogram from the day before. That is, for each parameter, the mean and CV from previously generated marginal posterior distribution is used to generate a new normal prior distribution for the next forecasting interval. The daily updated priors illustrate how well the Bayesian-based seismicity forecasting framework adapts to the seismic sequence daily, especially during the first two days. In general, unimodal and symmetric posterior densities are observed, in particular for the latter forecasting intervals after the second main shock. The mean posteriors are thus shown to

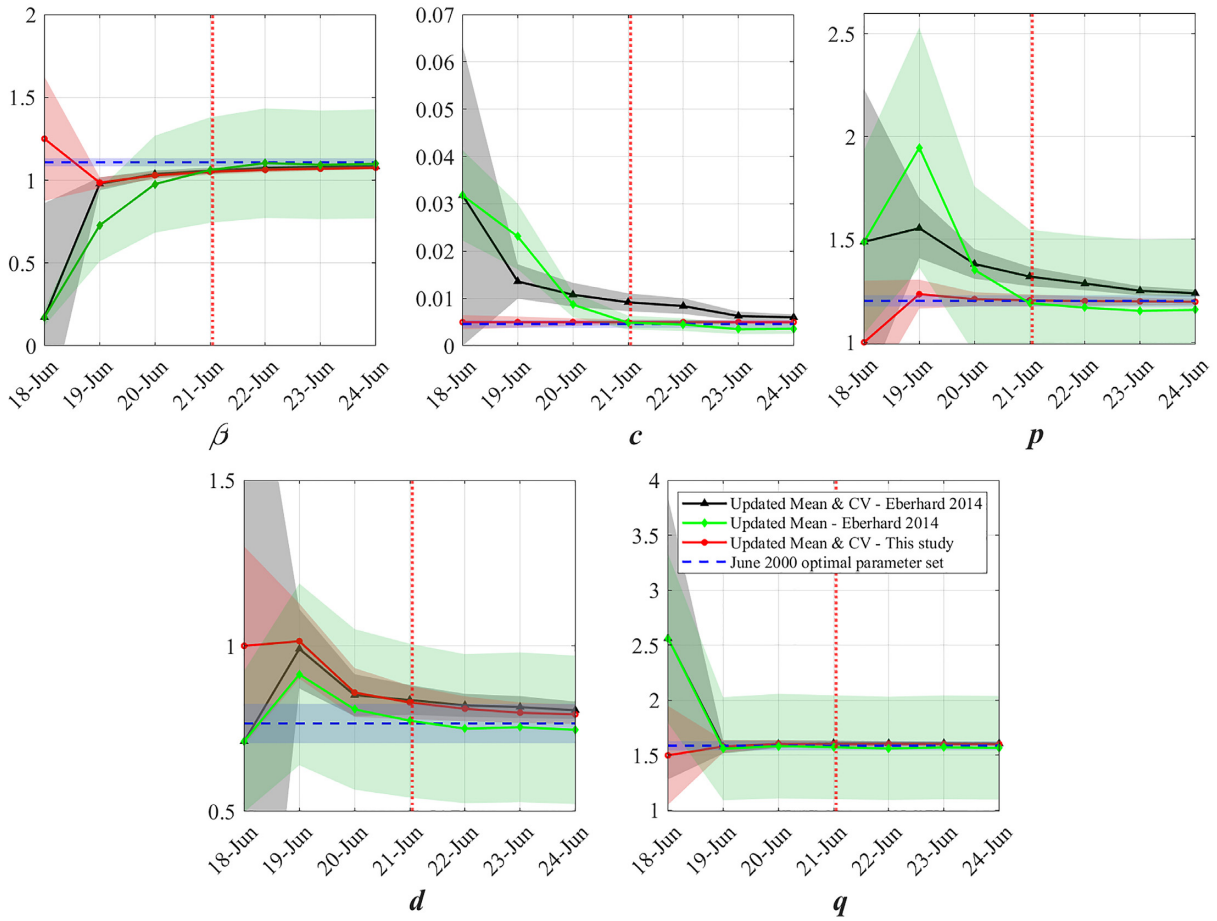

Figure 11. Comparison of three approaches of initial prior information (see legend) incorporated in the Bayesian ETAS parameter estimation procedure for daily forecasting intervals with T_{start} = 0:00 UTC from 18 June up to 24 June 2000. Mean values (symbols) and standard deviations (shaded area) are plotted by similar colours for each scenario. The blue dashed lines represent the optimal June 2000 sequence ETAS parameter set. The vertical red dotted line depicts the start point of the second sequence at 00:51 UTC on 21 June 2000.

converge towards a stable set of parameters with very low CVs, that progressively become smaller with time. Parenthetically we note that the distribution of K, K_R and K_t are derived from the other main five parameters.

4.5 Effects of different initial ETAS values on the posterior estimates

For the daily seismicity forecasts that start at every midnight from 18 to 24 June we used the mean and CV of the posterior distributions from the previous forecasting interval as prior information for each subsequent interval. The initial prior values for the main ETAS parameters are reported in the first column of Tables 1 and 2, also see Sections 4.2 and 4.3. In this way, the first forecasting interval is based on the best available estimates of model parameters and then the natural progression of the seismic sequence is allowed to progressively inform the Bayesian ETAS model for each subsequent forecasting interval. We show this progression as red lines in Fig. 11 for each parameter. As a reference, we show constant blue dashed lines in blue shaded areas (i.e. the posterior mean and standard deviation) for each parameter that were estimated via a retrospective inference using the *entire* seismic sequence from 17 to 24 June as **seq**. These values are $\beta = 1.108$ (CV $= 0.0226$), $c = 0.0046$ (CV $= 0.174$), $p = 1.20$ (CV $= 0.0225$), $d = 0.765$ (CV $= 0.077$), $q = 1.588$ (CV $= 0.0264$) and $K = 0.51$ (CV $= 0.14$). As expected, the daily updated values converge to values very close to those obtained by the analysis of the entire aftershock sequence (i.e. the last points of the red lines in Fig. 11 shown in the last column of Table 2 and the last row of posteriors in Fig. 10). Stating this differently, the red line is seen to converge towards the values of the blue dashed lines as the daily forecasting progresses, which was to be expected as progressively more information (both data and informed priors) are being used for later forecasting intervals. Correspondingly, the CV of the red line decreases rapidly with time. Overall, the reference mean values (blue dashed lines) can be considered as the optimal June 2000 sequence ETAS parameters and thereby, with reasonable CVs (e.g. 0.3), can be used as informative priors for Bayesian updating of seismicity forecasts during future seismic sequences.

We contrast this rapid parametric convergence of daily updates with that when using less than ideal starting values of unknown uncertainties, that is using the initial priors from the previous ETAS study for SW Iceland (Eberhard 2014). As they were presented without uncertainty measures, two scenarios have been considered: (1) we allow both the mean values and CVs to be updated daily while we assign

large values of CV to the first prior values allowing them to cover a wide range of probable values (black lines), on the other and (2) only allow the mean values to be update and keeping CV constant at 0.3 (green lines).

We observe that in both cases, despite the incredibly large differences between the initial values estimated in previous study and the more ideal initial parameters (see values associated with 18 June, especially for parameters β, c and q), the model learns effectively from the sequence through the Bayesian updating process incorporating updating prior estimation and consequently, the parameters reach convergence with the values from the other approaches. The β, c, p and d parameters tune themselves only over the first couple of forecasting intervals and converge towards the proposed sequence-based parameters. The temporal parameters (c and p) converge slower when the CV of the prior distribution is updated based on the previous posterior PDF than forcing a constant large CV throughout, in particular when the initial prior value is poor.

Overall, the result shows that as long as the prior values are selected in a reasonable range, the Bayesian updating procedure works perfectly towards well-determined posterior distributions which are generated gradually by increasing the amount of data. However, if the initial values are too far from the ideal values despite allowing for a large CV, the tuning process of the parameters during the MCMC routines are likely to be decelerated during an ongoing seismic sequence or/and they might trade-off with one another and as a result reach unrealistic estimate.

We observe that to attain reliable forecasts as fast as possible for future seismic sequences in the immediate aftermath of a strong earthquake, it is important to use an already established and informative set of Bayesian ETAS priors, and to update the priors for the next forecasting interval based on the posteriors of the previous one. According Fig. 11, the updates are especially important over approximately the first three days after a large main shock, the updating prior estimation can be stopped as the prior estimates are stable with trivial difference with the proposed optimal ETAS parameter set while maintaining their accuracy sufficiently.

4.6 Likelihood-based tests for evaluating forecasted seismicity

In this section, we thoroughly quantify the incorporated model assessment in the Collaboratory for the Study of Earthquake Predictability (CSEP) framework (Zechar *et al.* 2010; Taroni *et al.* 2014; Schorlemmer *et al.* 2018). To this end, we apply likelihood-based testing procedures such as L- and N-tests that isolate the spatial and magnitude component of a space–rate–magnitude forecast (Zechar *et al.* 2010).

N-test: The N-test verifies (in a probabilistic manner) whether the overall forecasted number of earthquakes is consistent with the observed number of target events over the entire region. According to this test, we fit a Poisson distribution to the forecasted number of target events $N_{\rm fore}$ with magnitude greater than a threshold, which is actually the expected number of events in the forecasting interval that we have estimated [see $\mathrm{E}[N(x, y, m|\mathbf{seq}, M_{\rm cut})]$ in eq. (3)]. Then, we measure if the observed number of events $N_{\rm obs}$ with magnitude greater than a threshold over the entire aftershock zone is not located in the tails of the Poisson distribution. To this end, the N-test results is presented by two quantile scores that should be greater than a critical threshold value of $P_{\rm eff}$:

$$\delta_1 = P\ (n \geq N_{\rm obs}|N_{\rm fore}) = 1 - P\ (n \leq N_{\rm obs} - 1|N_{\rm fore}) = 1 - \sum_{n\,=\,0}^{N_{\rm obs}-1} \frac{(N_{\rm fore})^n e^{-N_{\rm fore}}}{n!} \tag{11a}$$

$$\delta_2 = P\ (n \leq N_{\rm obs}|N_{\rm fore}) = \sum_{n=0}^{N_{\rm obs}} \frac{(N_{\rm fore})^n e^{-N_{\rm fore}}}{n!}, \tag{11b}$$

If one of these scores is below $P_{\rm eff}$, the forecast is deemed to be underpredicting ($\delta_1 \ll P_{\rm eff}$) or overpredicting ($\delta_2 \ll P_{\rm eff}$). The $P_{\rm eff}$ is set to 0.025 corresponding to the 95 per cent confidence interval.

It is worth noting that the Bayesian-based methodology performs already an advanced N-test in the sense that instead of assigning a Poisson distribution to the forecasted number of events, it directly estimates the distribution of the forecast and computes its percentiles (i.e. 50$^{\rm th}$, 16$^{\rm th}$, 84$^{\rm th}$, 2$^{\rm nd}$ and 98$^{\rm th}$) which are presented as error bars in each forecasting maps presented in Sections 4.2 and 4.3. In this way, one can realize how well the forecasted number of earthquakes matches $N_{\rm obs}$.

L-test: The L-test verifies whether the spatial occurrence of observed earthquakes is consistent with the forecasts of the model. In other words, it measures how well the forecast in a single spatial cell matches the observation in that spatial cell. According to this test, we calculate the joint log-likelihood of observations $N_{{\rm obs},n}$ given the forecasts $N_{{\rm fore},n}$, where $n = 1$: $N_{\rm grid}$, denoted as $L_{\rm obs}$ herein, in all cell units as follows:

$$L_{\rm obs} = \ln\left(\prod_{n=1}^{N_{\rm grid}} \frac{(N_{{\rm fore},n})^{N_{{\rm obs},n}} e^{-N_{{\rm fore},n}}}{N_{{\rm obs},n}!}\right) = \sum_{n=1}^{N_{\rm grid}} \left[-N_{{\rm fore},n} + N_{{\rm obs},n} \ln\left(N_{{\rm fore},n}\right) - \ln\left(N_{{\rm obs},n}!\right)\right]. \tag{12}$$

The L-test is basically consisted of two stages: (1) sample $N_{\rm sim}$ from a Poisson distribution with mean value equal to $N_{\rm fore}$; (2) for each N_{sim} simulated in the previous step, we sample a number between zero and unity (assuming a uniform distribution) in order to locate the event in the corresponding spatial cell according to the proportion of $N_{\rm fore}$ in the cell units (i.e. using the inverse cumulative distribution function). These two stages (repeated N times) lead to the construction of N simulated catalogues of events. Finally, for each of these N simulated catalogues, we calculate the joint log-likelihood of $N_{{\rm sim},n}$ simulations given the forecasts $N_{{\rm fore},n}$, where $n = 1$: $N_{\rm grid}$, denoted as $L_{\rm sim}$ herein,

Table 3. N- and L-test results for forecasting intervals during the June 2000 sequence.

Forecasting Intervals	Duration	5 hr	4 hr		24 hr			
	T_{start}	19:00 UTC 17-Jun	20:00 UTC 17-Jun	20:00 UTC 17-June∗	0:00 UTC 18-Jun	0:00 UTC 19-June	0:00 UTC 20-Jun	0:00 UTC 21-Jun
N-test (δ_1)		1	0.99	0.95	**0.0027**	0.39	0.516	0
N-test (δ_2)		**9.6e-07**	**0.0002**	0.05	0.997	0.66	0.568	1
L-test (γ)		0.98	0.99	0.92	0.31	0.303	0.68	0
Forecasting intervals	Duration	20 hr	18 hr	24 hr				
	T_{start}	4:00 UTC 21-June	6:00 UTC 21-June	6:00 UTC 21-June	6:00 UTC 22-Jun			
N-test (δ_1)		0.344	0.351	0.458	0.577			
N-test (δ_2)		0.705	0.705	0.59	0.507			
L-test (γ)		0.22	0.348	0.39	0.41			

∗ For all forecasting scenarios $M_{cut} = 2.0$, except this forecasting analysis in which M_{cut} is set to 1.5.

in all cell units as follows:

$$L_{\text{sim}} = \ln\left(\prod_{n=1}^{N_{\text{grid}}} \frac{(N_{\text{fore},n})^{N_{\text{sim},n}} e^{-N_{\text{fore},n}}}{N_{\text{sim},n}!}\right) = \sum_{n=1}^{N_{\text{grid}}} \left[-N_{\text{fore},n} + N_{sim,n} \ln(N_{\text{fore},n}) - \ln(N_{\text{sim},n}!)\right]. \tag{13}$$

Repeating the above procedure for each simulated catalogue (generated based on the procedure described above), we have a vector of joint log-likelihood L_{sim}. It is to note that the log-likelihoods L_{obs} and also L_{sim} has a negative value, and values that are closer to zero indicate a more likely observation. Let us estimate the probability that the log-likelihood L is smaller than L_{obs}, $P(L \leq L_{\text{obs}})$. If L_{obs} falls in the lower tail of the distribution, this indicates that the observation is not consistent with the forecast in each cell; thus, the forecast is not accurate. This probability can be estimated as follows:

$$\gamma = P(L \leq L_{\text{obs}}) = \frac{N(L_{\text{sim}} \leq L_{\text{obs}})}{N(L_{\text{sim}})}, \tag{14}$$

where the numerator indicates the number N of the components in the vector L_{sim} that are equal to or smaller than L_{obs}, and the denominator is the total number of elements in L_{sim} which is equal to the number of simulated catalogues in the reliability framework. If γ is below the critical threshold value that is usually adopted by the CSEP experiments, that is 0.05 corresponds to 5 per cent significance, the forecast is deemed to be inconsistent with the space-rate distribution of the observation. More technical details can be found in the study of Zechar *et al.* (2010).

In Table 3 we present the results of the N- and L-test for all forecasting intervals over the June 2000 seismic sequence investigated in Section 4.2 (Figs 6 and 7) and Section 4.3 (Figs 8 and 9) after the first and second main shocks, respectively. Bold underlined values indicate that the observed distribution is inconsistent with the forecast.

From the table, it can be seen that no forecast fails L-test indicating strong spatial forecasting ability of the Bayesian ETAS model, even in early aftershock period and over all following forecasting intervals. The δ_1 and δ_2 greater than 0.025 guaranty that the real case of N_{obs} will not be within the tails of our forecast. We note that all forecasts following the second main shock succeeded. In early forecasts after the 17 June main shock, δ_2 is estimated too small indicating an overprediction. This observation is apparent from their corresponding forecasts maps displayed in Figs 6(a) and (b) (see the error bars). In addition, an underprediction is exhibited for the first daily forecasting on 18 June which is consistent with the Fig. 7(a) forecasting map's result. Based on the δ_1 values, 21 June daily forecasts with $T_{\text{start}} = 00{:}00$ significantly underpredicted the total number of target earthquakes. This is expected as the second main shock with M_{w} 6.5 happened ∼1.0 hr after the time of issuing the forecast.

5 CONCLUSION

A spatio-temporal ETAS model has been calibrated to the 17–24 June 2000 seismic sequence in southwest Iceland. It uses a Bayesian parameter estimation technique that enables estimation of the ETAS model parameters while accounting for their uncertainties in a robust manner using MCMC simulation. The model has been used to generate maps of short-term seismicity forecasts of various start times and durations for the June 2000 seismic sequence with the purpose of investigating the reliability of the forecasts with respect to the observations, and the sensitivity of the model parameter estimates to initial assumptions. The seismicity forecasting maps were studied in the context of an OEF manner that monitoring agencies are faced with in practice and immediately after a main shock.

Starting with initial values from the literature as best prior estimates of the model parameters their inference was carried out over various forecasting intervals of maximum 24-hr duration, each resulting in new parametric estimates in the form of their posterior distributions. The

first forecasting intervals were set to start a few hours after the first main shock and were of relatively short duration, with later intervals each starting at midnight, set admittedly arbitrarily. Adaptive inference was used, that is where the posteriors from each preceding forecasting interval served as informative priors for the next one. The statistics of the posterior joint probability distribution of the ETAS model parameters sampled by the MCMC simulation algorithm along with the Markov chains were studied to evaluate the reliability and convergence of the inference. Reliable estimates confirmed by unimodal and symmetric posterior distributions for each ETAS parameter were observed for all forecasting intervals.

The forecasted spatio-temporal seismicity distribution of aftershocks larger than the cut-off magnitude $M_{\text{cut}} = 2.0$ was compared with the actual observations during each forecasting interval. The forecasting with respect to the total number of forecasted events improved remarkably when M_{cut} was manually lowered to 1.5 to allow the use of a richer parametric catalogue while the model exhibited a strong spatial forecasting ability, even only a few hours after the main shock, and over all subsequent intervals. The daily forecasts for successive interval then improved steadily using the adaptive inference approach manifested by the 16–84 percentile range of the forecasted number of events capturing the actual number of observed earthquakes. The exception is the 21 June forecasting interval where essentially a new sequence commenced after the occurrence of a second main shock of M_{w} 6.5, less than 1 hr after the start of the corresponding forecasting interval. By resetting the forecasting to start a few hours after the second main shock the 16–84 percentile levels of the forecasted number of events were again able to capture the observed number of earthquakes.

After adaptive inference progressively over all forecasting intervals, the final parametric values were obtained. They are in very good agreement with the model parameters inferred when retroactively analysing the 17–24 June 2000 sequence in its entirety. We present these sets of parameters as the representative ETAS parametric values for the June 2000 sequence. While they are slightly different compared with the parametric values found in the literature and that served as the initial values for the modelling, the model parameters converged very fast to these final values. We note that much slower convergence was observed when using less ideal initial values affecting the reliability of the first forecasting intervals. It is therefore important for any seismicity forecast of future sequences in the aftermath of a strong earthquake to use the best possible initial parametric values to ensure the reliability over the first forecasting intervals, with the adaptive inference ensuring the continued reliability over the latter intervals.

This study has provided us with a unique opportunity to gain more insight and understanding of the short-term earthquake forecasting capabilities of a seismicity forecasting framework for SW-Iceland, in the form of a calibrated spatio-temporal Bayesian ETAS model. Other Icelandic seismic sequences need to be analysed in a consistent manner and retrospectively, to evaluate the stability of the Bayesian ETAS parameters by seismic sequence, seismic region and then nationally. In addition, a quantitative comparison of the Bayesian ETAS forecasting model with forecasts of other conventional ETAS models calibrated to the same data need to be performed. Their focus would be the evaluation of the models' respective benefits and limits, along with proving an estimate of the epistemic uncertainty involved in ETAS seismicity forecasts—an important prerequisite for the operational application of ETAS seismicity forecasts in Iceland (e.g. Jalilian 2019; Ross 2021). We envision that the Bayesian ETAS model along with the optimal parameter set could thus potentially be applied as a regional operational earthquake forecasting system for aftershocks, enabled by the real-time magnitude and location capability of the SIL seismic system and its low magnitude of completeness. In turn, that would enable a short-term spatio-temporal probabilistic seismic hazard assessment for aftershocks which has practical importance as aftershocks can progressively cause increased damages and economic losses after a main shock, and effective post-event response is crucial to reduce such losses in an earthquake-stricken region.

ACKNOWLEDGMENTS

This study is a part of the TURNkey project (earthquake-turnkey.eu) (Towards more Earthquake-Resilient Urban Societies through a Multi-Sensor-Based Information System enabling Earthquake Forecasting, Early Warning and Rapid Response Actions), supported by the European Union's Horizon 2020 research and innovation programme under grant agreement No. 821046. This study was additionally supported by a Postdoctoral fellowship (#218255) from the Icelandic Research Fund of the Icelandic Centre for Research for the first author, the Icelandic Research Fund (#228782), and the RISE H2020 project (Real-time earthquake rIsk reduction for a reSilient Europe, rise-eu.org) supported the work of the last author. We would like to thank John Douglas for his helpful comments on an earlier version of this article and also the Editor, Dr Margarita Segou, Dr Mehdi Zare and the reviewers for their valuable comments which strongly improved the presentation and clarity of our findings.

DATA AVAILABILITY

The earthquake catalogue data underlying this paper are available at online Harvard dataverse via https://doi.org/10.7910/DVN/NUD9GI. The MATLAB scripts for the Bayesian ETAS model can be accessed on GitHub through the following link: https://github.com/HossEbi/Bayesian_spatiotemporal_ETAS_model_ver1

REFERENCES

Antonioli, A., Belardinelli, M.E., Bizzarri, A. & Vogfjord, K.S., 2006. Evidence of instantaneous dynamic triggering during the seismic sequence of year 2000 in south Iceland, *J. geophys. Res.,* **111,** doi:10.1029/2005JB003935.

Árnadóttir, T., 2004. Coseismic stress changes and crustal deformation on the Reykjanes Peninsula due to triggered earthquakes on 17 June 2000, *J. geophys. Res.,* **109**(9), doi:10.1029/2004JB003130.

Árnadóttir, T., Hreinsdóttir, S., Gudmundsson, G., Einarsson, P., Heinert, M. & Völksen, C., 2001. Crustal deformation measured by GPS in the South Iceland Seismic Zone due to two large earthquakes in June 2000, *Geophys. Res. Lett.,* **28,** 4031–4033.

Azarbakht, A., Ebrahimian, H., Jalayer, F. & Douglas, J., 2022. Variations in hazard during earthquake sequences between 1995 and 2018 in western Greece as evaluated by a Bayesian ETAS model, *Geophys. J. Int.,* **231,** 27–46.

Beck, J.L. & Au, S.-K., 2002. Bayesian updating of structural models and reliability using Markov chain Monte Carlo simulation, *J. Eng. Mech.,* **128,** 380–391.

Bellou, M., Bergerat, F., Angelier, J. & Homberg, C., 2005. Geometry and segmentation mechanisms of the surface traces associated with the 1912 Selsund Earthquake, Southern Iceland, *Tectonophysics,* **404,** 133–149.

Bjarnason, I.T., Cowie, P., Anders, M.H., Seeber, L. & Scholz, C.H., 1993. The 1912 Iceland earthquake rupture: growth and development of a nascent transform system, *Bull. seism. Soc. Am.,* **83,** 416–435.

Cao, A. & Gao, S.S., 2002. Temporal variation of seismic b-values beneath northeastern Japan island arc, *Geophys. Res. Lett.,* **29,** 48–41-48-3.

Console, R., Murru, M., Catalli, F. & Falcone, G., 2007. Real time forecasts through an earthquake clustering model constrained by the rate-and-state constitutive law: comparison with a purely stochastic ETAS model, *Seismol. Res. Lett.,* **78,** 49–56.

Console, R., Murru, M. & Falcone, G., 2010. Probability gains of an epidemic-type aftershock sequence model in retrospective forecasting of $M \geq 5$ earthquakes in Italy, *J. Seismol.,* **14,** 9–26.

Convertito, V., Ebrahimian, H., Amoroso, O., Jalayer, F., De Matteis, R. & Capuano, P., 2021. Time-dependent seismic hazard analysis for induced seismicity: the case of St Gallen (Switzerland), geothermal field, *Energies,* **14**(10), 2747, doi:10.3390/en14102747.

Darzi, A., Bessason, B., Halldorsson, B., Molina, S., Kharazian, A. & Moosapoor, M., 2022a. High spatial-resolution loss estimation using dense array strong-motion near-fault records. Case study for Hveragerði and the Mw 6.3 Ölfus earthquake, South Iceland, *Int. J. Disaster Risk Reduct.,* **73,** doi:10.1016/j.ijdrr.2022.102894.

Darzi, A., Halldorsson, B., Hrafnkelsson, B. & Vogfjörð, K.S., 2022b. Short-term Bayesian ETAS spatiotemporal forecasting of the Ölfus 2008 earthquake sequence in Iceland, *Tectonophysics,* **839,** doi:10.1016/j.tecto.2022.229522.

Douglas, J. & Azarbakht, A., 2020. Cost–benefit analyses to assess the potential of Operational Earthquake Forecasting prior to a mainshock in Europe, *Nat. Hazards,* **105,** 293–311.

Eberhard, D.A.J., 2014. *Multiscale Seismicity Analysis and Forecasting Examples from the Western Pacific and Iceland,* ETH Zurich.

Ebrahimian, H. & Jalayer, F., 2017. Robust seismicity forecasting based on Bayesian parameter estimation for epidemiological spatio-temporal aftershock clustering models, *Sci. Rep.,* **7,** 9803, doi:10.1038/s41598-017-09962-z.

Ebrahimian, H., Jalayer, F., Asprone, D., Lombardi, A.M., Marzocchi, W., Prota, A. & Manfredi, G., 2014. Adaptive daily forecasting of seismic aftershock hazard, *Bull. seism. Soc. Am.,* **104,** 145–161.

Ebrahimian, H. *et al.*, 2019. Site-specific probabilistic seismic hazard analysis for the western area of Naples, Italy, *Bull. Earthq. Eng,* **17,** 4743–4796.

Einarsson, P., 1991. Earthquakes and present-day tectonism in Iceland, *Tectonophysics,* **189,** 261–279.

Einarsson, P., 2010. Mapping of Holocene surface ruptures in the South Iceland Seismic Zone, *Jökull,* **60,** 121–138.

Einarsson, P., 2014. Mechanisms of earthquakes in Iceland, in *Encyclopedia of Earthquake Engineering,* eds Beer, M., Kougioumtzoglou, I.A., Patelli, E. & Au, I.S.-K., pp. 1–15, Springer Berlin Heidelberg.

Einarsson, P., Hjartardóttir, Á.R., Hreinsdóttir, S. & Imsland, P., 2020. The structure of seismogenic strike-slip faults in the eastern part of the Reykjanes Peninsula Oblique Rift, SW Iceland, *J. Volc. Geotherm. Res.,* **391,** 106372,.

Field, E.H. *et al.*, 2016. The potential uses of operational earthquake forecasting, *Seismol. Res. Lett.,* **87,** 313–322.

Field, E.H. *et al.*, 2017. A spatiotemporal clustering model for the third uniform California earthquake rupture forecast (UCERF3-ETAS): toward an operational earthquake forecast, *Bull. seism. Soc. Am.,* **107,** 1049–1081.

Godano, C., Lippiello, E. & Arcangelis, L. de., 2014. Variability of the b value in the Gutenberg–Richter distribution, *Geophys. J. Int.,* **199,** 1765–1771.

Gutenberg, B. & Richter, C.F., 1944. Frequency of earthquakes in California, *Bull. seism. Soc. Am.,* **34,** 185–188.

Hainzl, S., Christophersen, A. & Enescu, B., 2008. Impact of earthquake rupture extensions on parameter estimations of point-process models, *Bull. seism. Soc. Am.,* **98,** 2066–2072.

Hainzl, S., Zakharova, O. & Marsan, D., 2013. Impact of aseismic transients on the estimation of aftershock productivity parameters, *Bull. seism. Soc. Am.,* **103,** 1723–1732.

Hardebeck, J.L., Llenos, A.L., Michael, A.J., Page, M.T. & Elst, N. van der., 2019. Updated California aftershock parameters, *Seismol. Res. Lett.,* **90,** 262–270.

Harte, D.S., 2013. Bias in fitting the ETAS model: a case study based on New Zealand seismicity, *Geophys. J. Int.,* **192,** 390–412.

Harte, D.S., 2014. An ETAS model with varying productivity rates, *Geophys. J. Int.,* **198,** 270–284.

Harte, D.S., 2017. Probability distribution of forecasts based on the ETAS model, *Geophys. J. Int.,* **210,** 90–104.

Harte, D.S., 2019. Bias in fitting the ETAS model: a case study based on New Zealand seismicity, *Geophys. J. Int.,* **192,** 390–412.

Hastings, W.K., 1970. Monte Carlo sampling methods using Markov chains and their applications, *Biometrika,* **57,** 97–109.

Hjaltadóttir, S., 2009. Use of relatively located microearthquakes to map fault patterns and estimate the thickness of the brittle crust in Southwest Iceland. Sub-surface fault mapping in Southwest Iceland, *MS thesis*. Retrieved from https://skemman.is/handle/1946/3990.

Jalayer, F., Asprone, D., Prota, A. & Manfredi, G., 2011. A decision support system for post-earthquake reliability assessment of structures subjected to aftershocks: an application to L'Aquila earthquake, 2009, *Bull. Earthq. Eng.,* **9,** 997–1014.

Jalayer, F. & Ebrahimian, H., 2014. MCMC-based updating of an epidemiological temporal aftershock forecasting model, *vulnerability, uncertainty, and risk*, in *Presented at the Second International Conference on Vulnerability and Risk Analysis and Management (ICVRAM) and the Sixth International Symposium on Uncertainty, Modeling, and Analysis (ISUMA),* American Society of Civil Engineers, Liverpool, UK, pp. 2093–2103.

Jalilian, A., 2019. ETAS: an R package for fitting the space-time ETAS model to earthquake data, *J. Stat. Software,* **88**(1), 1–39.

Jónasson, K., Bessason, B., Helgadóttir, Á., Einarsson, P., Guðmundsson, G.B., Brandsdóttir, B., Vogfjörd, K.S. & Jónsdóttir, K., 2021. A harmonized instrumental earthquake catalog for Iceland and the northern Mid-Atlantic Ridge, *Nat. Hazards Earth Syst. Sci.,* **21,** 2197–2214.

Jordan, T.H. *et al.*, 2011. Operational earthquake forecasting: state of knowledge and guidelines for utilization, *Ann. Geophys.,* **54,** 319–391.

Kolev, A.A. & Ross, G.J., 2019. Inference for ETAS models with non-Poissonian mainshock arrival times, *Stat. Comput.,* **29,** 915–931.

Llenos, A.L. & Michael, A.J., 2017. Forecasting the (un)productivity of the 2014 M 6.0 South Napa aftershock sequence, *Seismol. Res. Lett.,* **88,** 1241–1251.

Lombardi, A.M., 2017. The epistemic and aleatory uncertainties of the ETAS-type models: an application to the Central Italy seismicity, *Sci. Rep.,* **7,** 11812, doi:10.1038/s41598-017-11925-3.

Marzocchi, W. & Lombardi, A.M., 2009. Real-time forecasting following a damaging earthquake, *Geophys. Res. Lett.,* **36,** 1–5.

Marzocchi, W., Lombardi, A.M. & Casarotti, E., 2014. The establishment of an operational earthquake forecasting system in Italy, *Seismol. Res. Lett.,* **85,** 961–969.

Marzocchi, W., Taroni, M. & Falcone, G., 2017. Earthquake forecasting during the complex Amatrice-Norcia seismic sequence, *Sci. Adv.,* **3,** 1–8.

Metropolis, N., Rosenbluth, A.W., Rosenbluth, M.N., Teller, A.H. & Teller, E., 1953. Equation of state calculations by fast computing machines, *J. Chem. Phys.,* **21,** 1087–1092.

Metzger, S. & Jónsson, S., 2014. Plate boundary deformation in North Iceland during 1992–2009 revealed by InSAR time-series analysis and GPS, *Tectonophysics,* **634,** 127–138.

Nandan, S., Ouillon, G., Sornette, D. & Wiemer, S., 2019. Forecasting the rates of future aftershocks of all generations is essential to develop better earthquake forecast models, *J. geophys. Res.,* **124**(8), 8404–8425.

Nanjo, K.Z., Sakai, S., Kato, A., Tsuruoka, H. & Hirata, N., 2013. Time-dependent earthquake probability calculations for Southern Kanto after the 2011 M9.0 Tohoku earthquake, *Geophys. J. Int.,* **193,** 914–919.

Ogata, Y., 1998. Space-time point-process models for earthquake occurrences, *Ann. Instit. Stat. Math.,* **50,** 379–402.

Ogata, Y. & Katsura, K., 2006. Immediate and updated forecasting of aftershock hazard, *Geophys. Res. Lett.,* **33,** doi:10.1029/2006GL025888.

Ogata, Y., Katsura, K., Falcone, G., Nanjo, K. & Zhuang, J., 2013. Comprehensive and topical evaluations of earthquake forecasts in terms of number, time, space, and magnitude, *Bull. seism. Soc. Am.,* **103,** 1692–1708.

Omi, T., Ogata, Y., Hirata, Y. & Aihara, K., 2013. Forecasting large aftershocks within one day after the main shock, *Sci. Rep.,* **3,** 2218, doi:10.1038/srep02218.

Omi, T., Ogata, Y., Hirata, Y. & Aihara, K., 2014. Estimating the ETAS model from an early aftershock sequence: omi et al.: estimating the ETAS model, *Geophys. Res. Lett.,* **41,** 850–857.

Omori, F., 1894. On the aftershocks of earthquake, *J. Coll. Sci. Imp. Univ. Tokyo,* **7,** 111–200.

Page, M.T., Elst, Der, van, N., Hardebeck, J., Felzer, K. & Michael, A.J., 2016. Three ingredients for improved global aftershock forecasts: tectonic region, time-dependent catalog incompleteness, and intersequence variability, *Bull. seism. Soc. Am.,* **106,** 2290–2301.

Pagli, C., Pedersen, R., Sigmundsson, F. & Feigl, K.L., 2003. Triggered fault slip on June 17, 2000 on the Reykjanes Peninsula, SWIceland captured by radar interferometry, *Geophys. Res. Lett.,* **30**(6), 1273, doi:10.1029/2002GL015310.

Panzera, F., Zechar, J.D., Vogfjörd, K.S. & Eberhard, D.A.J., 2016. A revised earthquake catalogue for South Iceland, *Pure appl. Geophys.,* **173,** 97–116.

Papadopoulos, A.N., Bazzurro, P. & Marzocchi, W., 2021. Exploring probabilistic seismic risk assessment accounting for seismicity clustering and damage accumulation: part I. Hazard analysis, *Earthq. Spectra,* **37,** 803–826.

Pedersen, R., Jónsson, S., Árnadóttir, T., Sigmundsson, F. & Feigl, K.L., 2003. Fault slip distribution of two June 2000 MW6.5 earthquakes in South Iceland estimated from joint inversion of InSAR and GPS measurements, *Earth planet. Sci. Lett.,* **213,** 487–502.

Reasenberg, P.A. & Jones, L.M., 1989. Earthquake hazard after a mainshock in California, *Science,* **243,** 1173–1176.

Rögnvaldsson, S.T., Guðmundsson, Á. & Slunga, R., 1998. Seismotectonic analysis of the Tjörnes Fracture Zone, an active transform fault in north Iceland, *J. geophys. Res.,* **103,** 30 117–30 129.

Ross, G.J., 2021. Bayesian estimation of the ETAS model for earthquake occurrences, *Bull. seism. Soc. Am.,* **8,** 1473–1480.

Roth, F., 2004. Stress changes modelled for the sequence of strong earthquakes in the South Iceland seismic zone since 1706, in *Geodetic and Geophysical Effects Associated with Seismic and Volcanic Hazards,* Pageoph Topical Volumes, pp. 1305–1327, ed. Fernández, J., Birkhäuser.

Schorlemmer, D. *et al.*, 2018. The collaboratory for the study of earthquake predictability: achievements and priorities, *Seismol. Res. Lett.,* **89,** 1305–1313.

Seif, S., Mignan, A., Zechar, J.D., Werner, M.J. & Wiemer, S., 2017. Estimating ETAS: the effects of truncation, missing data, and model assumptions, *J. geophys. Res.,* **122,** 449–469.

Shcherbakov, R., Zhuang, J. & Ogata, Y., 2018. Constraining the magnitude of the largest event in a foreshock–main shock–aftershock sequence, *Geophys. J. Int.,* **212,** 1–13.

Shcherbakov, R., Zhuang, J., Zöller, G. & Ogata, Y., 2019. Forecasting the magnitude of the largest expected earthquake, *Nat. Commun.,* **10,** 4051, doi:10.1038/s41467-019-11958-4.

Sigbjörnsson, R. & Ólafsson, S., 2004. On the South Iceland earthquakes in June 2000: strong-motion effects and damage, *Bollettino di Geofisica Teorica edApplicata,* **45,** 131–152.

Sigmundsson, F., 2006. *Iceland Geodynamics: Crustal Deformation and Divergent Plate Tectonics,* Springer Science & Business Media.

Sigmundsson, F., Einarsson, P., Bilham, R. & Sturkell, E., 1995. Rift-transform kinematics in south Iceland: deformation from Global Positioning System measurements, 1986 to 1992, *J. geophys. Res.,* **100,** 6235–6248.

Standards Council of Iceland /Staðlaráð Íslands (SI)., 2010. *Icelandic National Annexes to EUROCODES (No. ÍST EN 1998-2004/NA:2010),* Staðlaráð Íslands, Reykjavík, Iceland.

Stefánsson, R., 2020. Useful predictions ahead of large earthquakes and lessons learned for future progress, *Geod. Geodyn.,* **11,** 1–17.

Stefánsson, R. *et al.*, 1993. Earthquake prediction research in the South Iceland seismic zone and the SIL project, *Bull. seism. Soc. Am.,* **83,** 696–716.

Stefánsson, R., Guðmundsson, G.B. & Halldórsson, P., 2008. Tjörnes fracture zone. New and old seismic evidences for the link between the North Iceland rift zone and the Mid-Atlantic ridge, *Tectonophysics,* **447,** 117–126.

Steigerwald, L., Einarsson, P. & Hjartardóttir, Á.R., 2020. Fault kinematics at the Hengill triple junction, SW-Iceland, derived from surface fracture pattern, *J. Volc. Geotherm. Res.,* **391,** 106439, doi:10.1016/j.jvolgeores.2018.08.017.

Taroni, M., Zechar, J.D. & Marzocchi, W., 2014. Assessing annual global M6+ seismicity forecasts, *Geophys. J. Int.,* **196,** 422–431.

Taroni, M. *et al.*, 2018. Prospective CSEP evaluation of 1-day, 3-month, and 5-yr earthquake forecasts for Italy, *Seismol. Res. Lett.,* **89,** 1251–1261.

Utsu, T., 1961. A statistical study on the occurrence of aftershocks, *Geophys. Mag.,* **30,** 521–605.

Utsu, T. & Ogata, Y., 1995. The centenary of the Omori formula for a decay law of aftershock activity, *J. Phys. Earth,* **43,** 1–33.

Zechar, J.D., Gerstenberger, M.C. & Rhoades, D.A., 2010. Likelihood-based tests for evaluating space-rate-magnitude earthquake forecasts, **100,** 1184–1195.

Zhuang, J., Ogata, Y. & Vere-Jones, D., 2002. Stochastic declustering of space-time earthquake occurrences, *J. Am. Stat. Assoc.,* **97,** 369–380.

SUPPORTING INFORMATION

Supplementary data are available at *GJI* online.

Table S1. Statistics (mean and coefficient of variation, CV) of marginal posterior distribution of ETAS parameters using different number of MCMC samples.

Figure S1. Prior (blue curves) and histogram of sampled posteriors of the main ETAS parameters associated with 10000 MCMC iterations.

Figure S2. From left to right: Trace plots of posterior samples of the main ETAS model parameters, [β, c, p, d, q], using 220 (top panel), 2000 and 10000 (bottom panel), and five chains within MCMC simulations (left) with the initial 10 per cent of iterations during the burn-in period indicated in grey colour. The corresponding posterior histograms (grey bars) and their associated statistics (red solid and red dashed lines). The Gelman–Rubin convergence statistics w.r.t sampling iterations (3rd column from left). The autocorrelation function plots are depicted by dark grey bars (right-hand panels). The results correspond to the 24-hr forecasting interval of 21 June 2000.

Please note: Oxford University Press is not responsible for the content or functionality of any supporting materials supplied by the authors. Any queries (other than missing material) should be directed to the corresponding author for the paper.